J. Fluid Mech. (1994), *vol.* 265, *pp.* 125–159

The spin-up of fluid in a rectangular container with a sloping bottom

By G. J. F. VAN HEIJST[1], L. R. M. MAAS[2] AND C. W. M. WILLIAMS[1]

[1] Department of Technical Physics, Eindhoven University of Technology, PO Box 513, 5600 MB Eindhoven, The Netherlands

[2] Netherlands Institute for Sea Research, PO Box 59, 1790 AB Den Burg, Texel, The Netherlands

(Received 16 October 1992 and in revised form 6 October 1993)

The spin-up from rest of a homogeneous free-surface fluid contained in a rectangular tank with an inclined bottom has been studied in the laboratory. As in the case of a tank without bottom topography, it is found that in the spin-up process leading to the ultimate state of rigid-body rotation a number of stages can be distinguished, these being (i) the starting flow, characterized by zero absolute vorticity, (ii) the viscous generation of cyclonic vorticity at the lateral tank walls, leading to flow separation, and (iii) the formation of cyclonic and anticyclonic flow cells, which show a complicated interaction. When the topography steepness is small, these cells become organized in a regular array similar to what is observed in the non-sloping bottom case. For steeper topography, however, no organization into a regular cellular pattern is observed, and the relative fluid motion remains unsteady and irregular until eventually it has decayed owing to the spin-up/spin-down mechanism provided by the Ekman layer at the tank bottom. During the first stage of the adjustment process the starting flow takes on the appearance of a large anticyclonic cell that fills the fluid domain entirely. Depending on the ratio of the horizontal and vertical lengthscales of the tank this cell is either symmetric or asymmetric, with a higher density of streamlines in the deeper part of the tank. The coupled vorticity equation, governing the depth-independent part of the starting flow, and the potential equation describing its depth-dependent part have been solved analytically, and the comparison between these results and observational data is generally good.

1. Introduction

The process through which a viscous fluid in a rotating system adjusts to a change in the boundary conditions is commonly referred to as spin-up. It is a very common but quite complex phenomenon that involves many disparate temporal and spatial scales. Apart from their occurrence in many industrial situations (for example in rotating reactor vessels, turbomachinery, centrifuges for separation of mixtures), spin-up processes are relevant to a variety of geophysical and astrophysical situations. For example, through the efficient spin-up mechanism time-varying wind stresses exerted at the ocean's surface can induce flows in the ocean interior on timescales that are much shorter than those predicted by a purely diffusive balance. Another example is the so-called 'solar spin-down', caused by the continuous emission of matter by the Sun. The 'solar wind' carries away an amount of angular momentum, which results in a gradual spin-down of the Sun. The outer layers are in a state of turbulent convection, and the efficient mixing mechanism associated with this state results in a rapid distribution of

the angular momentum loss over the Sun's outer layers. Because such an efficient mixing mechanism is not available in the deep interior, it has been postulated that the Sun's interior is rotating more rapidly than the visible surface layers. For a clear description of this solar spin-down process as well as some other spin-up phenomena the reader is referred to the useful review paper by Benton & Clark (1974).

In general the term 'spin-up' describes the flow adjustment process to a state of solid-body rotation with an ultimate rotation rate Ω that is higher than the initial rate Ω_0, whereas the term 'spin-down' is commonly used for the case $\Omega < \Omega_0$. The spin-up problem of a homogeneous fluid in a closed axisymmetric cylindrical tank rotating about its axis was first described analytically by Greenspan & Howard (1963) for the linear case $\Omega = \Omega_0 + \Delta\Omega$, with $\Delta\Omega/\Omega_0 \ll 1$. They pointed out that, after changing the rotation rate, thin viscous Ekman layers form at the horizontal boundaries of the spinning tank on a timescale of $O(\Omega^{-1})$. These Ekman layers drive a meridional circulation in the inviscid interior, which brings interior fluid from larger radii to smaller radii, thus providing an efficient spin-up mechanism: since the angular momentum of the interior fluid is conserved (viscous effects are negligible in the interior on this timescale), the fluid in a ring of decreasing radius acquires a larger azimuthal velocity. In this way the fluid gradually spins up to a new state of solid-body rotation with the new angular velocity Ω. The spin-up time required to reach this state is of $O(E^{-\frac{1}{2}}\Omega^{-1})$, where $E = \nu/\Omega H^2$ is the Ekman number of the flow, with ν the kinematic viscosity and H the half-depth of the fluid in the tank. After this spin-up stage is completed, some small residual inertial oscillations may occur in the interior. These are gradually damped by viscous effects, on the much larger diffusive timescale of $O(E^{-1}\Omega^{-1})$. This ultimate viscous adjustment forms only a minor part of the complete spin-up process, and because the actual flow adjustment to the new rotation rate is basically completed at the end of the second state, the practical spin-up timescale is $T = E^{-\frac{1}{2}}\Omega^{-1}$.

The process of flow adjustment to a small increment in the rotation rate ($\Delta\Omega/\Omega \ll 1$) is commonly referred to as *linear* spin-up. It was found in later studies, see for instance Weidman (1976*a*, *b*), that the spin-up timescale derived for this case also applies to nonlinear cases, like for example the spin-up from rest ($\Delta\Omega/\Omega = 1$).

The majority of previous studies on fluid spin-up were restricted to axisymmetric tank geometries, the most common one being the axisymmetric cylinder with a rigid lid. Recently, the spin-up of a homogeneous free-surface fluid was studied by van Heijst (1989) for a variety of non-axisymmetric configurations, including an annulus with a radial barrier and a semi-circular cylinder. In such geometries, it was found that the flow adjustment to solid-body rotation is characterized by three distinct stages: (i) the zero-vorticity starting flow, (ii) the viscous production of vorticity at the lateral tank walls, leading to flow separation, and (iii) a subsequent organization into a regular cellular pattern, followed by a gradual decay of the relative flow due to the bottom Ekman layer. Except for the stage of flow separation, during most of the spin-up process the motion in the interior was observed to be approximately two-dimensional. A follow-up study by van Heijst, Davies & Davis (1990, hereinafter referred to as vHDD) concerned the spin-up from rest of a fluid in a rectangular tank, and laboratory experiments were performed with free-surface and rigid-lid upper boundary conditions, with both homogeneous and linearly stratified fluids. Again, the flow evolution was characterized by the three principle stages. As in the geometries examined by van Heijst (1989), the starting flow generally has the appearance of a single anticyclonic cell that fills the flow domain completely. The structure of this starting flow can be described analytically, under the assumption that the absolute vorticity of the flow is still zero at

this stage; the theoretical results show a perfect agreement with the observed velocity field.

In the next stage, the flow separation due to the cyclonic velocity production at the tank walls gives the flow a somewhat irregular appearance. This irregular flow behaviour quickly disappears, however, and the growth of flow cells is observed. Obviously, the width of the rectangular tank puts a physical limit on the cell growth, and ultimately the cells become arranged in a linear array, with alternating circulations. The number of cells in this organized stage was found to depend essentially on the length-to-width ratio (δ) of the container. In the free-surface case, the number of cells was always odd, irrespective of the value of δ, with a cyclonic cell positioned in the centre of the tank. This latter phenomenon was attributed to the drift induced by the parabolically shaped upper surface of the fluid, which tends to bring cyclonic vortices radially inwards, while anticyclonic vortices show a tendency to drift to deeper parts of the flow domain.

As an extension to the previous investigation (vHDD), the present study considers the effect of bottom topography. In particular, attention is concentrated on the spin-up of a homogeneous free-surface fluid in a rectangular container with a sloping bottom. Before any experiments were carried out, it was anticipated that the bottom topography could seriously affect the flow in the various stages of the spin-up process, and that sufficiently steep bottom slopes could possibly even prevent the flow from becoming organized in a cellular array. The laboratory experiments have confirmed this general conjecture, although it was found that for specific values of the geometry parameters the flow evolution was somewhat more complicated than originally anticipated.

The paper is organized as follows. The laboratory arrangement used for the experimental work is described in §2, and a general description of the laboratory observations is presented in §3. Next, the starting flow is analysed in §4. The vorticity equation governing the depth-independent part of this flow is more complicated than for the flat-bottom case, in the sense that it contains an extra symmetry-breaking term similar to that describing the β-effect in wind-driven or inertial ocean circulation models. A comparison of some analytical results and the laboratory observations of the starting flow is given in §5. That section also describes observational results concerning the flow in the later stages of the adjustment process. In particular, the relation between the relevant geometry parameters and the occurrence (or non-occurrence) of flow organization is considered. Another interesting effect addressed in that section is the non-uniformity of the spin-up timescale over the flow domain: in the case of a steep bottom slope this may lead to a relatively rapid spin-up in the shallow parts of the tank, while the relative motions in the deeper parts persist much longer. Finally, a general discussion of the results is presented in §6.

2. The experimental arrangement

The spin-up of a free-surface fluid in a rectangular tank was studied in the laboratory by use of a turntable whose rotation speed Ω was continuously adjustable from 0 to approximately 2 rad s^{-1}. The rectangular container, of horizontal dimensions L and B, was mounted concentrically, i.e. with its centre on the rotation axis of the turntable, and was filled with a homogeneous fluid (tap water) to a certain depth H. The tank contained a false flat bottom with some prescribed slope relative to the horizontal plane. For reference purposes it is useful to define a Cartesian coordinate system (x, y) in a horizontal plane, as indicated in figure 1. In all experiments described in

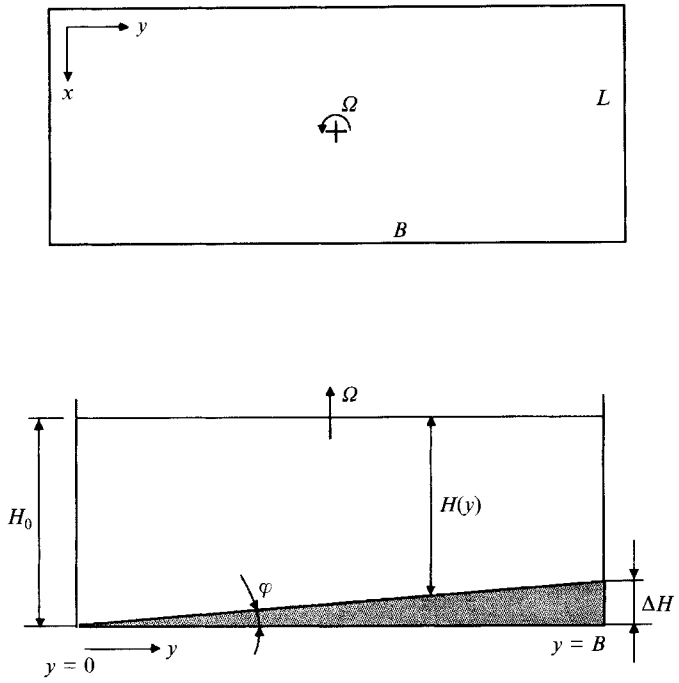

FIGURE 1. Definition sketch of the flow geometry.

this paper, the bottom was inclined in the lengthwise direction, i.e. in the y-direction, so that fluid depth is dependent on only one coordinate: $H = H(y)$. As indicated in figure 1, the largest depth (at $y = 0$) is H_0, whereas at the shallowest side ($y = B$) the depth is $H_0 - \Delta H$. It is convenient to define the following geometry parameters:

horizontal aspect ratio	$\delta = B/L,$	(1 *a*)
vertical aspect ratio	$\gamma = H_0/L,$	(1 *b*)
depth ratio	$\alpha = \Delta H/H_0,$	(1 *c*)
bottom slope	$\tan\varphi = \Delta H/B,$	(1 *d*)
rotational Froude number	$F = 4\Omega^2 B^2/(gH_0).$	(1 *e*)

In the present study attention is mainly restricted to cases in which $B > L$, i.e. to horizontal aspect ratios larger than unity ($\delta > 1$), although a few experiments have been carried out for $B \leqslant L$. The container that was used in the experiments had the following dimensions: $B = 89$ cm, $L = 39$ cm and a working depth of 25 cm. In most cases the length B of the tank was kept at this value and, by mounting two false sidewalls into the tank, the width of the fluid domain could be reduced continuously in order to cover a range of δ-values. For practical reasons, however, only the cases $\delta = 2.28$, 3.0, 4.0 and 5.0 will be shown. The depth ratio α was varied in the range 0 to 1. In fact, $\alpha = 0$ corresponds to a flat horizontal bottom, and the spin-up in that case has been discussed in vHDD. The other extreme value, $\alpha = 1$, corresponds with the case in which the depth in the shallowest part of the tank is exactly zero ($\Delta H = H_0$). By definition the bottom slope $\tan\varphi = \alpha\gamma/\delta$, and its value was varied in the range 0 to 0.18.

Prior to each experiment, the fluid was completely at rest relative to the non-rotating ($\Omega = 0$) container. Then, at $t = 0$ the table was set in rotation, and its angular velocity was gradually brought to some prescribed value $\Omega > 0$. In the experiments described in the present paper the ultimate rotation speed had a fixed value $\Omega = 0.556$ rad s^{-1},

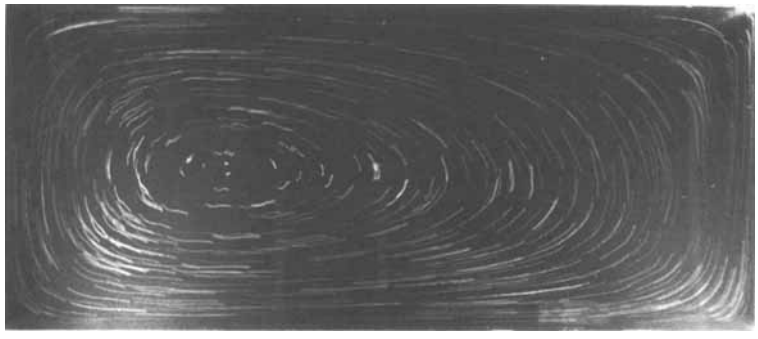

FIGURE 2. Streak photograph showing the starting flow of a homogeneous free-surface fluid in a rectangular tank with a sloping bottom that is spun-up from rest. Experimental parameters: $\delta = 2.28$, $\gamma = 0.34$, $\alpha = 0.92$ and the rotation period $T = 11.3$ s. The photograph was taken with exposure time 1 s.

and the duration of the table acceleration was approximately 3 s. It should be remarked that the flow is slowly rotating in the sense that the Rossby radius $(gH)^{\frac{1}{2}}/(2\Omega)$ is generally much larger than L. As in our earlier studies (van Heijst 1989; vHDD), the subsequent motion of the fluid was visualized by addition of small tracer particles, floating on the free surface of the fluid. The relative motions of these particles were recorded by a remotely controlled photo camera mounted in the rotating frame at some distance above the free surface. Streak photography (time exposures) enabled us – in addition to visualizing the large-scale flow patterns – to measure velocity distributions along characteristic cross-sections.

It should be noted that, strictly, the floating tracer particles only yield information about the flow at the free surface. In cases of pronounced bottom topographies it may thus be expected that the particle motions are not representative of the fluid flow at lower levels. In a few additional experiments, however, the flow was also visualized by vertical dye lines (produced by dropping $KMnO_4$ crystals in the fluid), which yielded information about the vertical structure of the flow field.

3. Observations

As discussed in vHDD, the spin-up of fluid in a rectangular tank with a flat, horizontal bottom is characterized by a number of stages. The first stage corresponds to the starting flow, which takes on the appearance of a large anticyclonic cell, filling the domain completely. For the case of a horizontal bottom, this cell is completely symmetric and its centre coincides with the centre ($x = \frac{1}{2}L, y = \frac{1}{2}B$) of the flow domain. In strong contrast, the starting cell in the sloping-bottom case is asymmetric, with its centre shifted towards the deeper side of the tank, as can be clearly seen in figure 2. It is obvious from the figure that the asymmetry in the streak pattern is most manifest in the direction of the topography gradient, although some less pronounced asymmetry with respect to the axis $x = \frac{1}{2}L$ can be observed in the shallow part of the flow region (on the right in figure 2). It was found that the principle asymmetry in the starting flow pattern (that in the y-direction) is much weaker for larger values of the horizontal aspect ratio δ. In fact, it is almost absent in the cases $\delta = 3$ and 4 that will be discussed below.

In the next stage of the spin-up process, the viscous production of cyclonic vorticity in the boundary layers at the lateral tank walls comes into play. This vorticity is

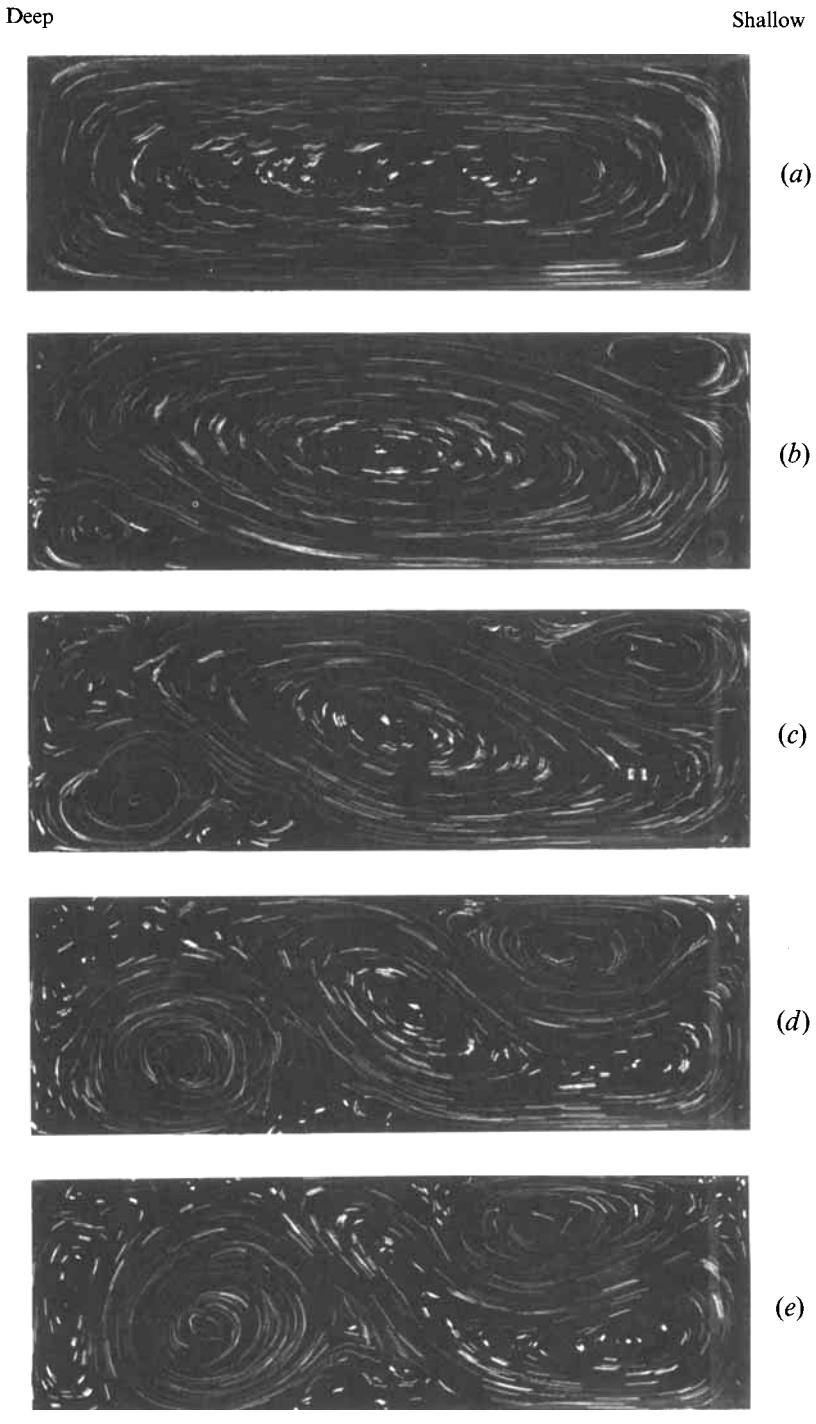

FIGURE 3(*a–e*). For caption see facing page.

advected by the main flow in a retrograde direction, and is generally found to accumulate in smaller cyclonic cells in the corner regions of the flow domain. This phenomenon is clearly observed in figure 3, which shows streakline pictures taken during the spin-up in a tank with horizontal aspect ratio $\delta = 3$ and depth ratio $\alpha = \frac{2}{3}$.

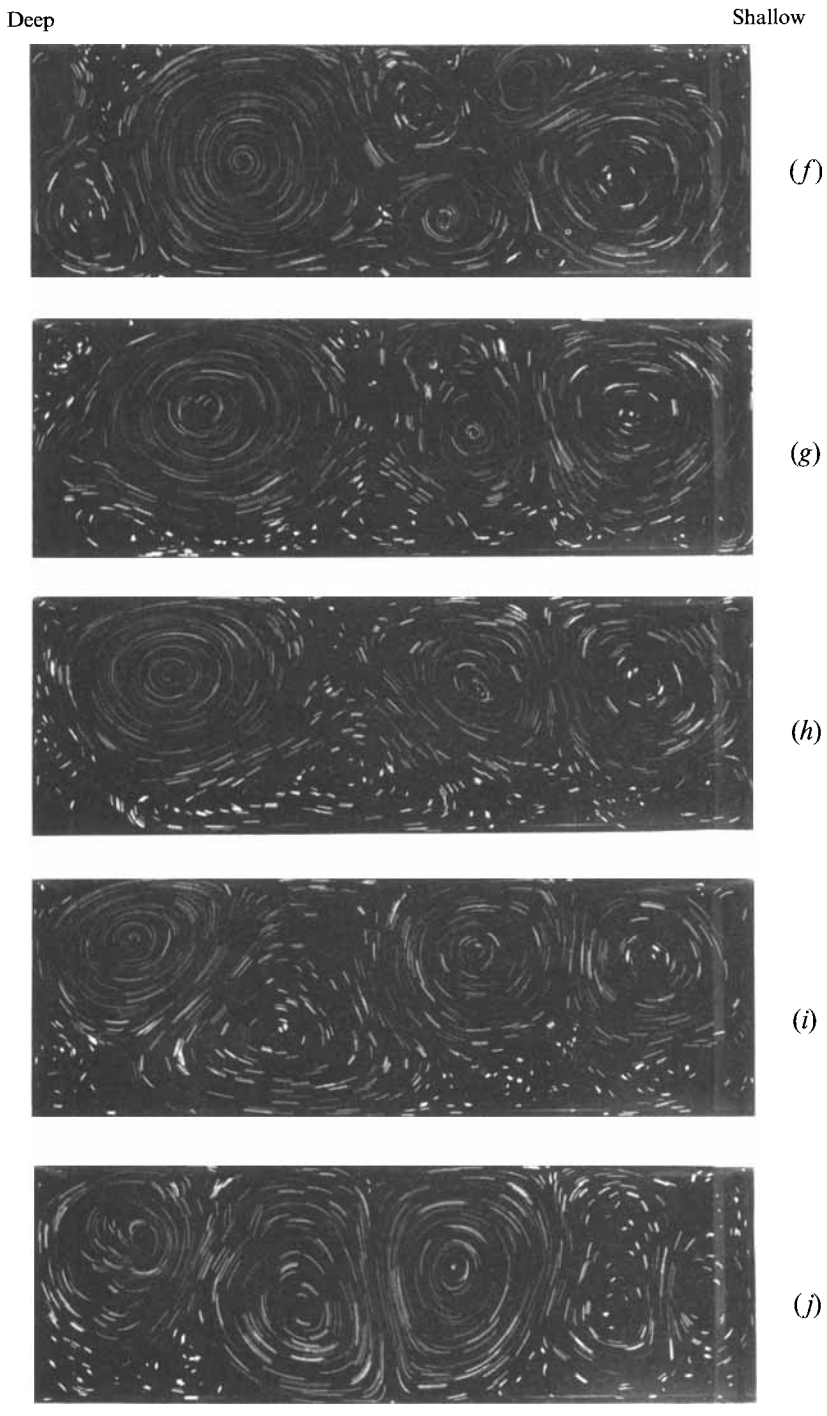

FIGURE 3. Sequence of plan-view photographs taken during the spin-up from rest of a homogeneous free-surface fluid in a rectangular container with a sloping bottom, with $\delta = 3$, $\gamma = 0.81$ and $\alpha = 0.66$. The flow is visualized by tracer particles floating on the fluid surface. The photographs were taken at (*a*) $t = 0.1T$, (*b*) $0.7T$, (*c*) $1.1T$, (*d*) $1.4T$, (*e*) $1.8T$, (*f*) $2.7T$, (*g*) $3.5T$, (*h*) $4.0T$, (*i*) $4.4T$ and (*j*) $8.0T$, with $T = 11.3$ s the rotation period. The exposure time was 1 s for (*a–i*) and 2 s for (*j*).

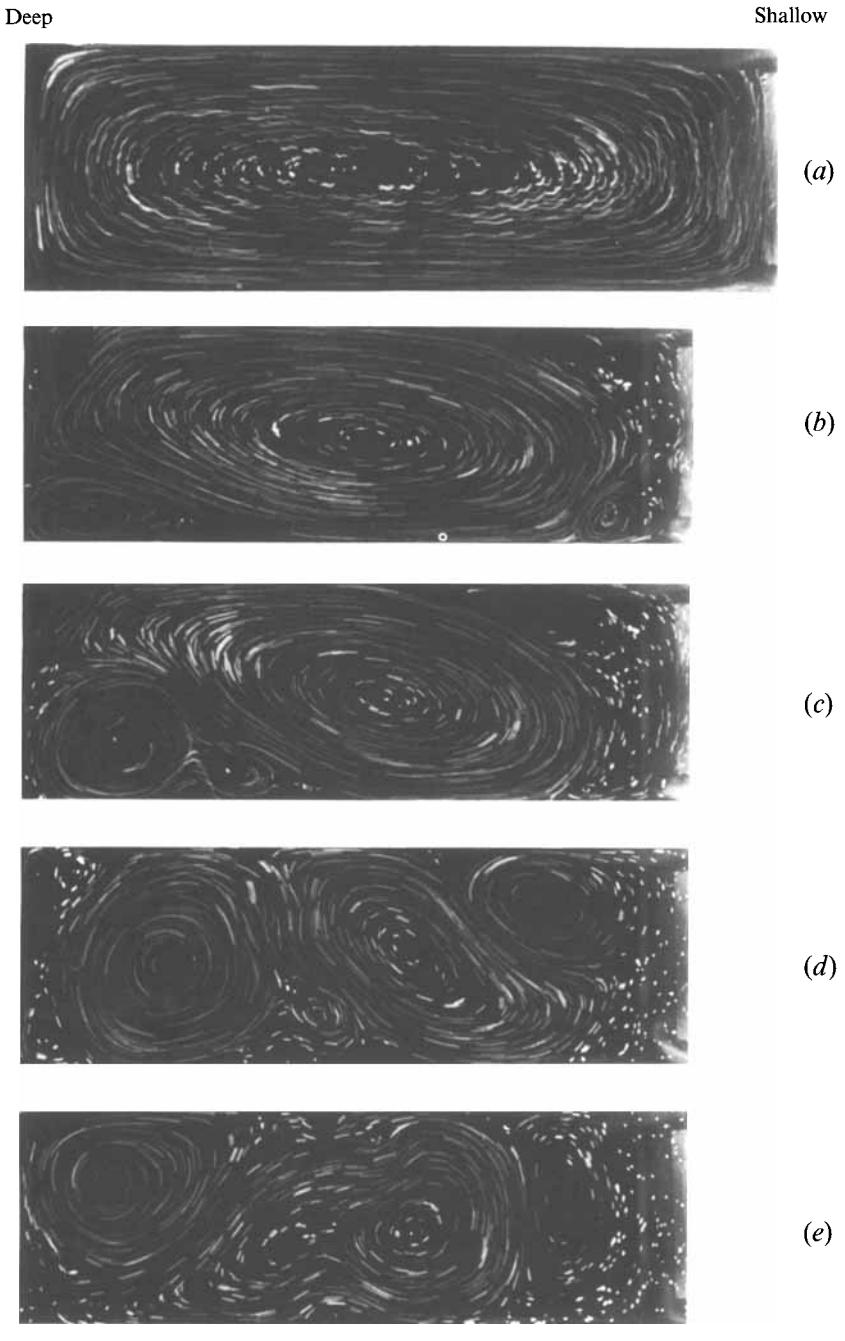

FIGURE 4(*a–e*). For caption see facing page.

As remarked before, the starting flow cell (figure 3*a*) is much less asymmetric in this case than in the case $\delta = 2.28$ (figure 2). In the next frame (figure 3*b*) the growth of cyclonic corner cells can clearly be seen: larger cells at the downstream ends of the longer sidewalls, and smaller cells at the downstream ends of the endwalls. The larger cyclonic cells show a rapid growth, while the smaller ones seem to vanish very quickly

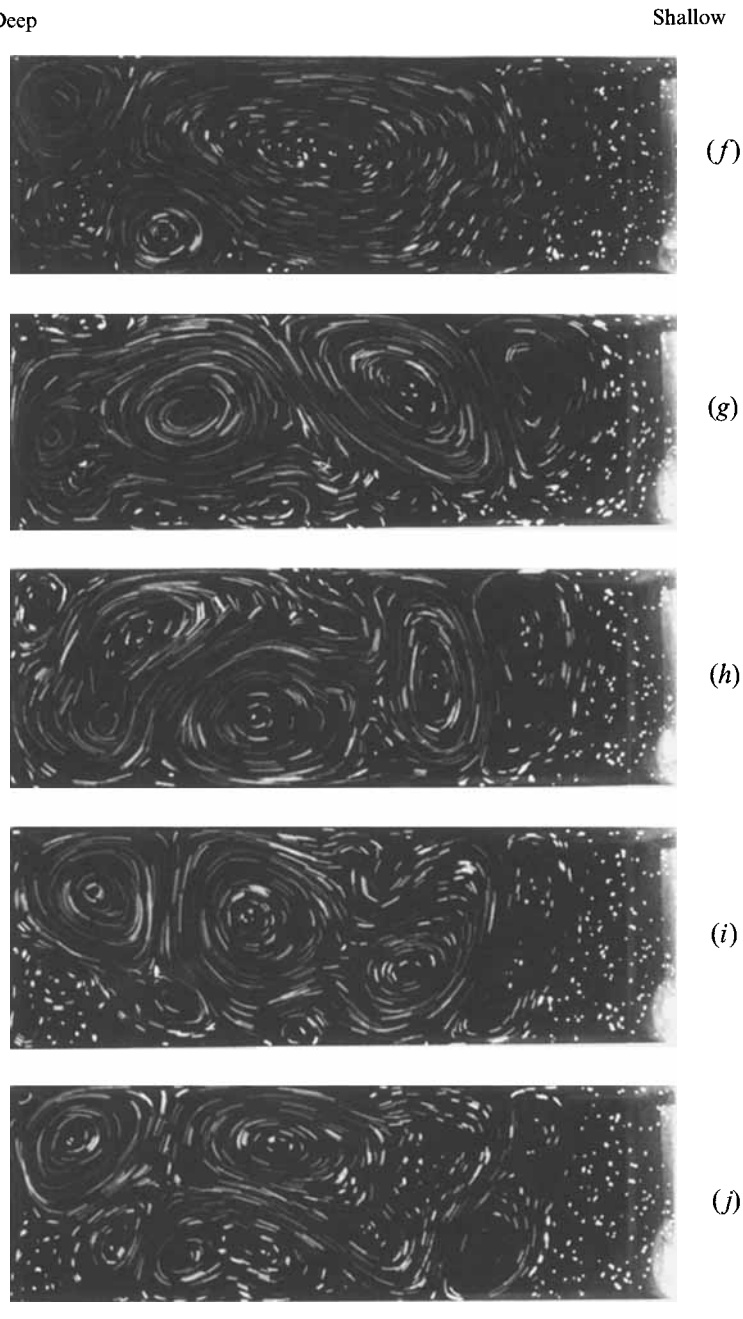

FIGURE 4. As figure 3, but now with $\gamma = 0.54$ and $\alpha = 0.98$. The photographs were taken at (*a*) $t = 0.1T$, (*b*) $0.7T$, (*c*) $1.1T$, (*d*) $1.8T$, (*e*) $2.8T$, (*f*) $3.9T$, (*g*) $5.3T$, (*h*) $6.2T$, (*i*) $7.1T$ and (*j*) $8.0T$, with $T = 11.3$ s. The exposure time was 1 s for (*a–f*) and 2 s for (*g–j*).

(see figure 3*c*). Up to this stage the flow evolution is very similar to the flat-bottom case (see figure 1 of vHDD). In the next stages, the original anticyclonic cell is observed to be pinched by the steadily growing corner cells, but in a definitely non-symmetric way (see figure 3*d*, *e*): the pinching results in a large anticyclonic cell in the shallow end of

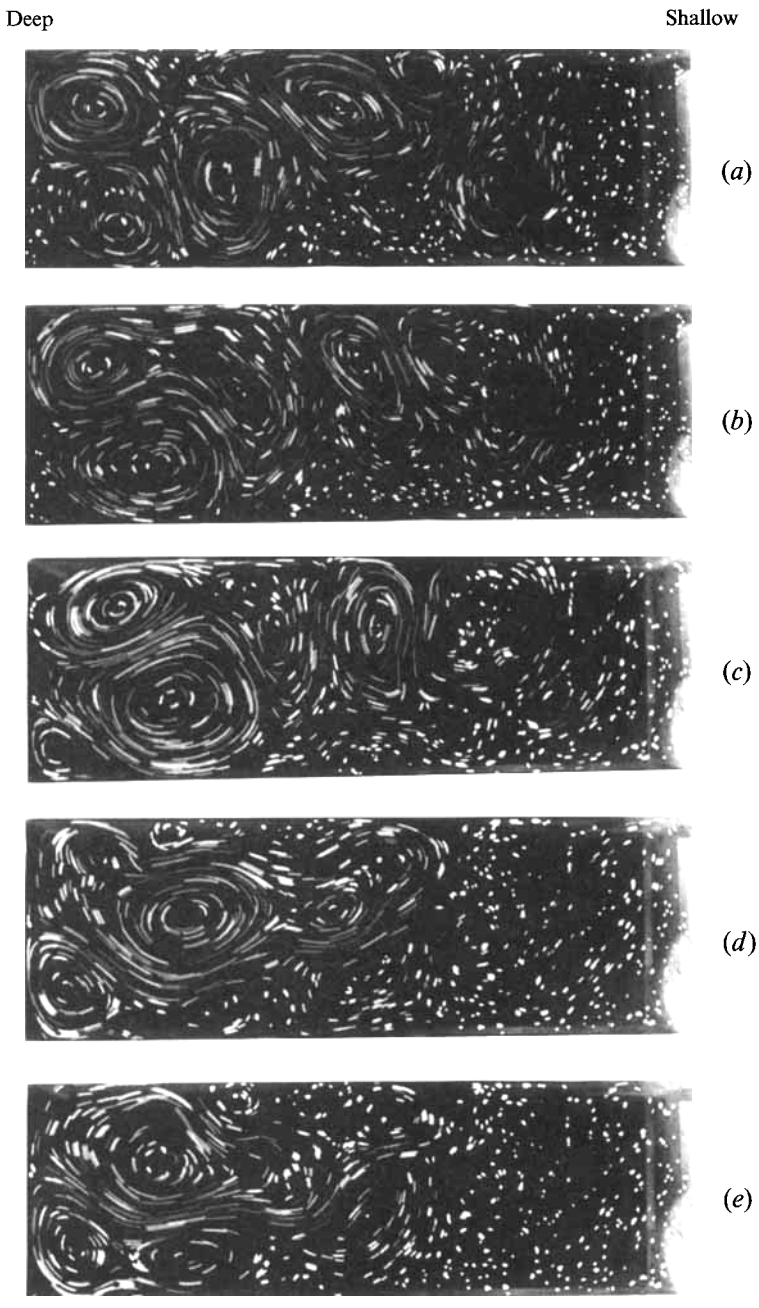

FIGURE 5(*a–e*). For caption see facing page.

the tank, and two smaller anticyclonic cells near the tank centre and near the deeper end, respectively (see figure 3*f*). In the subsequent frames (figure 3*g–j*) one observes a gradual rearrangement of the flow into a more or less regular pattern with alternately cyclonic and anticyclonic cells. Although some minor deformations of the cells do occur (compare figures 3*i* and 3*j*), the pattern itself was found to be stable and to persist until all relative motions had decayed due to the Ekman layer at the bottom of

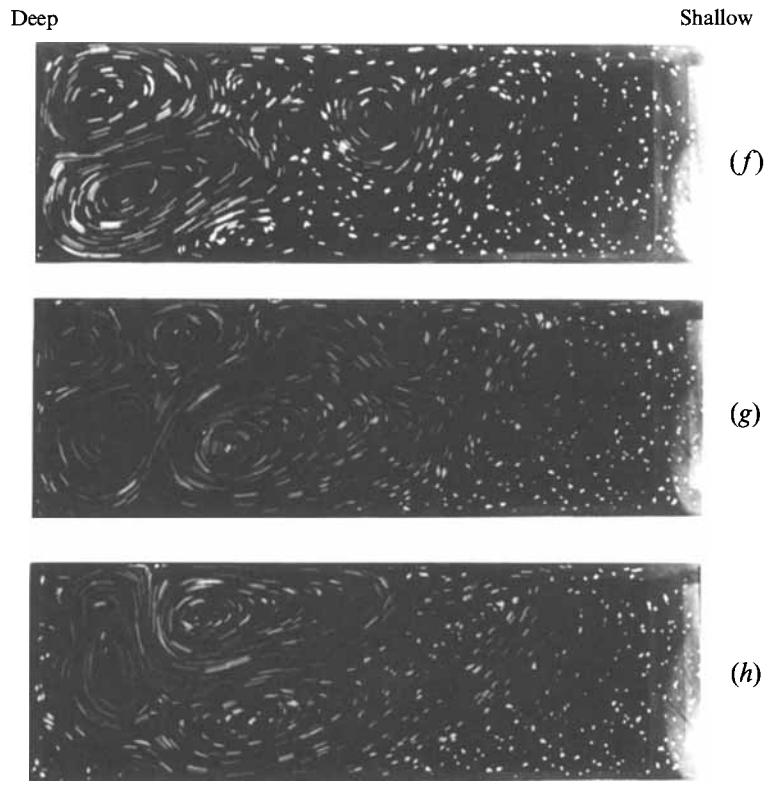

FIGURE 5. Continuation of the experiment shown in figure 4. The photographs were taken at (*a*) $t = 8.9T$, (*b*) $9.7T$, (*c*) $10.6T$, (*d*) $12.4T$, (*e*) $13.3T$, (*f*) $15.0T$, (*g*) $16.8T$ and (*h*) $19.5T$, with $T = 11.3$ s. The exposure time was (*a–b*) 2 s, (*c–f*) 3 s, (*g*) 4 s and (*h*) 5 s.

each cell. The eventual formation of cells was also found in the flat-bottom case, but with one major difference: in the present case ($\delta = 3$) with the sloping bottom the number of cells in the quasi-ultimate stage is $n = 4$ (the small cyclonic cell at the shallow end at the right of figure 3*j* was observed to disappear quickly), whereas in the flat-bottom case $\delta = 3$ this number appeared to be $n = 3$, with a cyclonic cell in the centre. The reason for this difference most probably lies in the asymmetric flow evolution prior to the pattern formation, and also in the behaviour of individual cells above topography, as will be discussed later in this section.

Figure 4 shows a similar experiment with aspect ratio $\delta = 3$, but now with a depth ratio $\alpha = 0.98$: the fluid depth at the right-hand sides of the photographs in that figure is almost zero. The major effect of this steeper bottom topography is immediate from the flow evolution. Although the starting-flow pattern is very similar to the one in figure 3, the subsequent growth of cyclonic cells in the corners of the domain is different from the small-α scenario: it is clearly seen in figure 4(*b*, *c*) that essentially one cyclonic cell is formed, namely in the deep part of the flow domain, at the downstream end of the long sidewall. This can be understood by considering a vertical vortex tube that is advected by the main flow along the lateral walls, in the retrograde direction. The stretching of the cyclonic-vorticity tube moving in the boundary layer into the deeper part of the tank results in an intensification of vorticity and therewith in a relatively strong cyclonic cell. On the other hand, a vortex tube moving in the boundary

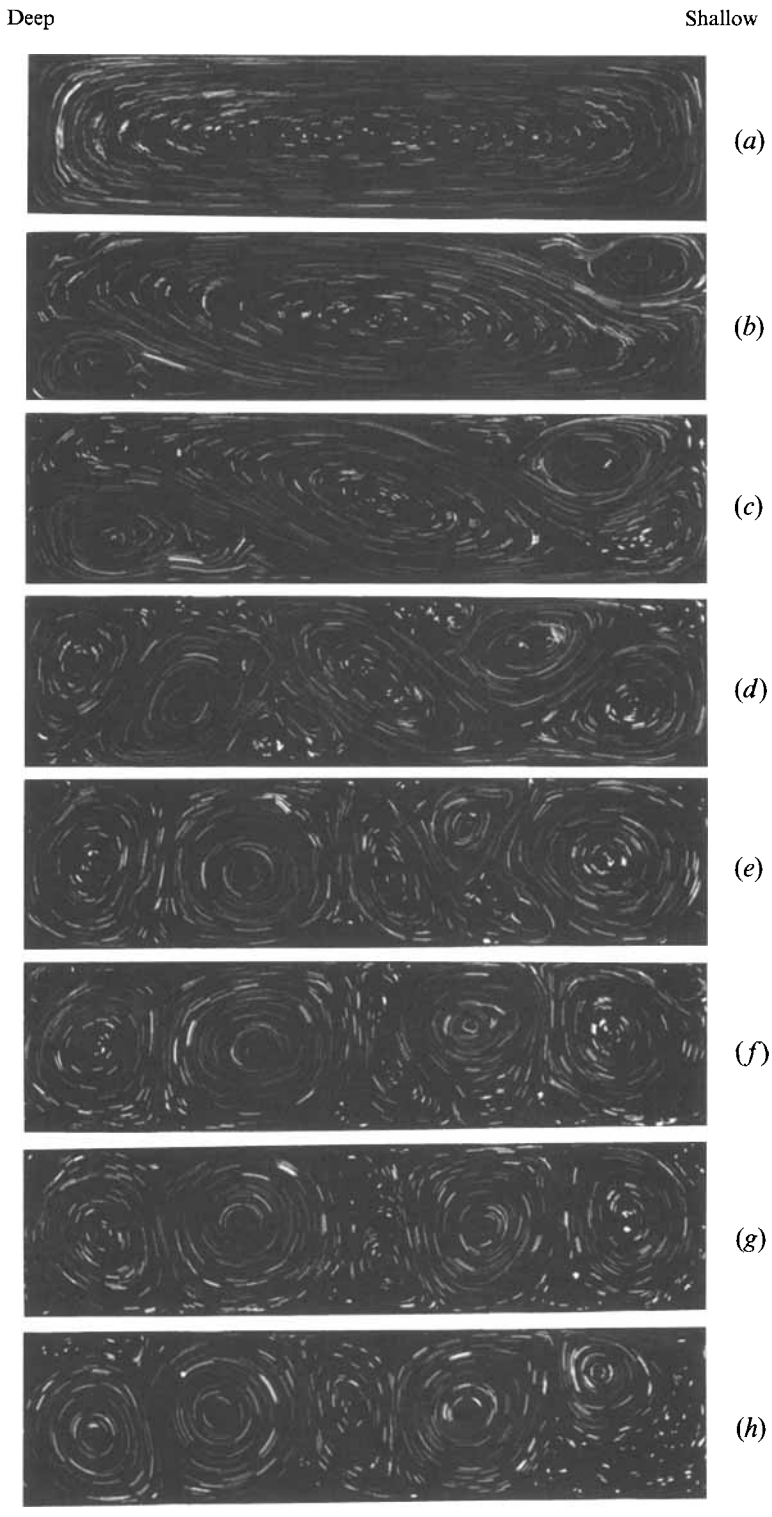

FIGURE 6. As figure 3, but now with $\delta = 4$, $\gamma = 0.72$, $\alpha = 0.5$ and $\tan\varphi = 0.09$. The photographs were taken at (*a*) $t = 0.1T$, (*b*) $0.9T$, (*c*) $1.3T$, (*d*) $1.8T$, (*e*) $2.7T$, (*f*) $3.1T$, (*g*) $4.0T$ and (*h*) $9.7T$, with $T = 11.3$ s. The exposure time was 1 s for (*a–g*) and 2 s for (*h*).

layer along the opposite tank wall is gradually squeezed while entering the shallow part of the flow domain, which counteracts the viscous production of cyclonic vorticity in the boundary layer. As a result, only a very weak cyclonic cell (or no cell at all) is formed in the shallow downstream end of that sidewall. This nicely illustrates how the stretching/compression of vortex tubes moving over bottom topography may dynamically intensify or weaken the vorticity generated by viscous effects in the lateral boundary layers.

Within a few rotation periods the flow seems to have formed a pattern of three cells (figure 4*d*), but this configuration is not stable, as can be concluded from the subsequent irregular flow patterns (figure 4*e–j*). The last picture of this sequence was taken at the same time ($t = 8.0T$, with $T = 11.3$ s the rotation period) as figure 3(*j*), but the flow does not show any formation of a regular, cellular pattern. Figure 5 shows a sequence of photographs illustrating the further evolution of the relative flow, from which it can be seen that the flow does not reach a quasi-steady state. The vortices keep on interacting in a complicated fashion, and a continuous process of merging and splitting of cells is observed. Also, at irregular intervals new cells are formed along the lateral boundaries of the flow domain. This phenomenon is attributed to the viscous generation of vorticity in the boundary layers.

Another striking feature of the flow evolution in this $\alpha \approx 1$ case (figures 4 and 5), when compared to the small-α case (figure 3), is the rapid decay of relative motion in the shallow part of the tank, which is obviously due to the Ekman layer at the sloping bottom. Although the unsteady Ekman layer has a very complicated structure in the present case, it is anticipated that the characteristic decay timescale associated with the spin-up/spin-down mechanism provided by the Ekman layer applies to the present case:

$$T_E = 2H/(\nu\Omega)^{-\frac{1}{2}}, \tag{2}$$

with H the local depth of the free-surface fluid, and ν the kinematic fluid viscosity. Since ν and Ω are constants, whereas H is a function of the upslope coordinate y, the effective decay timescale is a function of this coordinate as well. More specifically, in the case of an inclined bottom with a constant slope in the y-direction, the decay timescale of the relative motion is linearly dependent on y. This feature will be discussed in more detail in § 5.3.

It should be remarked that in the ultimate stage of cell formation, either in a regular or in an irregular pattern (as in cases with relatively steep topography, see e.g. figure 5), the flow is to a good approximation two-dimensional, as can be concluded from the absence of any substantial distortion or tilting of vertical dye lines that were produced by dropping $KMnO_4$ crystals in the fluid.

Additional experiments were carried out for the case with horizontal aspect ratio $\delta = 4$, both for weak ($\alpha = 0.5$) and strong ($\alpha = 0.89$) topographies. Figure 6 shows the flow evolution for the former case, which appears to be very similar to the weak-topography case ($\alpha = \frac{2}{3}$) illustrated by figure 3. The only main difference is that the pinching of the central anticyclonic cell is now much more symmetric (see figure 6*c–e*), and almost similar to what can be observed in the flat-bottom case ($\alpha = 0$; see figure 1 of vHDD).

Within typically 5 rotation periods of the turntable the flow is seen to become organized into a regular array of five cells (figure 6*g*, *h*) of alternate signs, with an anticyclonic cell in the centre. This configuration turned out to be stable, and the cells remained intact until the relative flow in the cells had completely decayed due to the

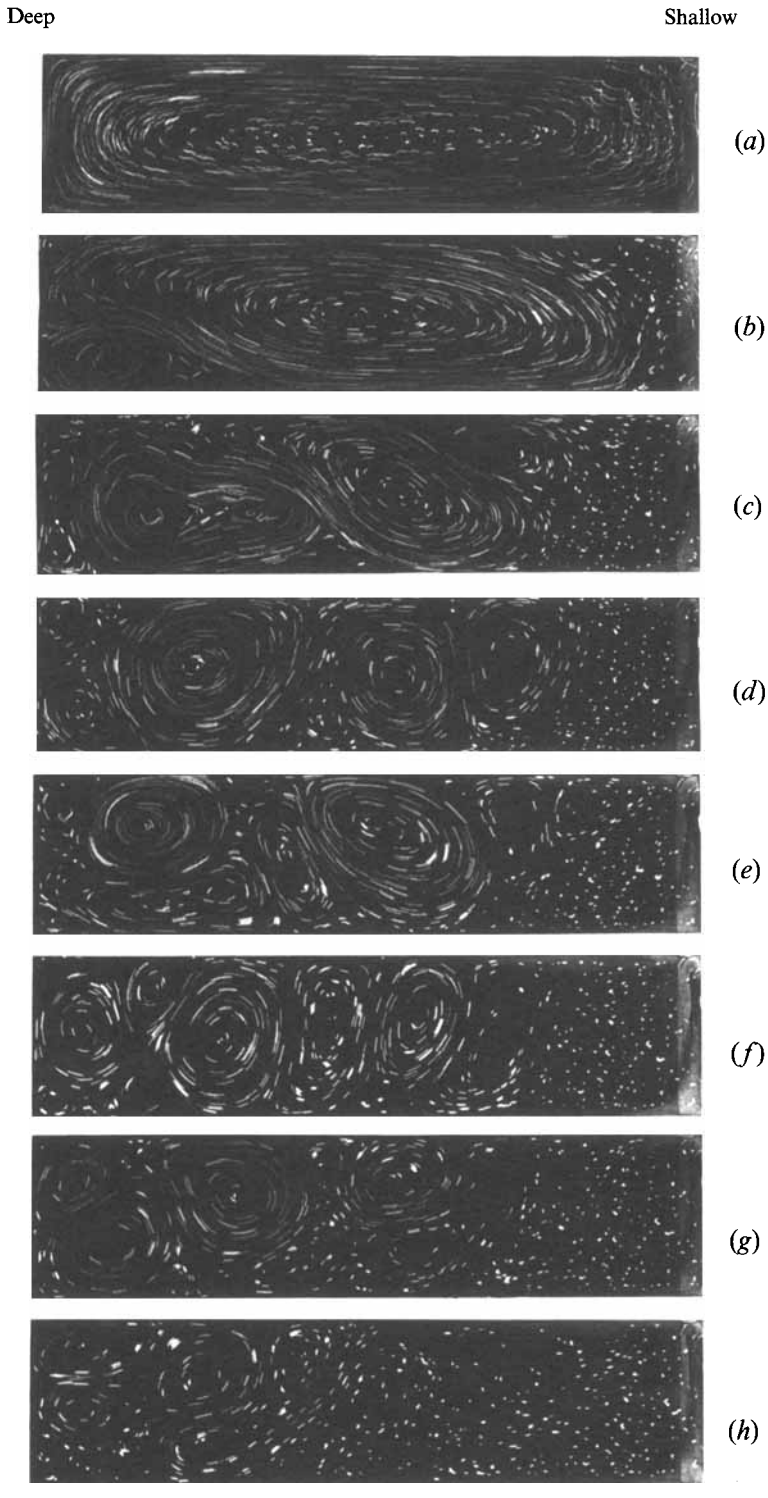

FIGURE 7. As figure 6, but now with $\gamma = 0.40$ and $\alpha = 0.89$. The photographs were taken at (*a*) $t = 0.1T$, (*b*) $0.9T$, (*c*) $1.8T$, (*d*) $3.1T$, (*e*) $4.9T$, (*f*) $7.1T$, (*g*) $9.7T$ and (*h*) $15.9T$, with $T = 11.3$ s. The exposure time was (*a–d*) 1 s (*e, f*) 2 s, (*g*) 3 s and (*h*) 5 s.

bottom Ekman layer. The evolution of the flow in the $\delta = 4$ case with relatively steep topography ($\alpha = 0.89$) is illustrated by figure 7, which shows *grosso modo* the same features as observed in the experiment with $\delta = 3$, $\alpha \approx 1$ (see figures 4 and 5): (i) the anticyclonic cell of the starting flow is more or less symmetric (figure 7); (ii) only one cyclonic corner cell is generated, viz. in the deeper part at the downstream end of the longer sidewall (figure 7*b*); (iii) the subsequent evolution of the flow is highly irregular, without showing any tendency to establish an organized pattern of cells; (iv) again, the relative flow in the shallow part of the flow domain shows a rapid decay, as a result of the decreased Ekman timescale (2) for shallower depths.

4. Analysis of the starting flow

In the initial stage of the spin-up problem the flow will be inviscid. This implies that the vorticity as observed from an inertial frame of reference will remain zero and the flow is essentially a potential flow. In a frame co-rotating with the tank the relative vorticity is just equal, but opposite, to the uniform value 2Ω of the tank.

In a flat-bottomed tank the flow consists of a single clockwise gyre, symmetric about the axes of symmetry of the tank (assumed to be rectangular in this study). Assuming that the free-surface remains essentially flat (such that there is no forcing of vertical motions) and assuming the fluid to be incompressible (such that a stream function can be introduced) the flow in the rotating frame of reference is determined by the conservation of vorticity, leading to a single Poisson equation for the stream function (see vHDD). When the bottom of the rectangular tank is sloping, however, the symmetric flow induces an upward vertical mass flux in that half of the tank where the flow is upslope, and a downward mass flux in the other half (see figure 8). These vertical mass fluxes are connected by an alongslope horizontal mass flux having the shallow side at its left (for a tank rotating anticlockwise). The height above the bottom to which this mass flux penetrates is determined by the vertical aspect ratio γ. For large values of $\gamma^2 (\gg 1)$ it is bottom trapped and the mass is returned in a shallow layer above the bottom, whereas for small values of this aspect ratio ($\gamma^2 \ll 1$) it extends throughout the fluid, right up to the surface, leading to a vertically uniform horizontal alongslope mass flux. This additional topographically induced flow component moves the stagnation point (the centre of the gyre) towards the deeper part: a symmetry breaking of the surface circulation pattern which is clearly a function of the vertical aspect ratio γ.

In the next subsection (§4.1) we consider the equations that govern the flow in the initial spin-up phase. As remarked in §3 the observed flow in most stages of the spin-up process is very close to two-dimensional – such as is expected to occur in a shallow tank ($\gamma^2 \ll 1$). For this reason, in §4.2, we treat the case that the topographically induced vertical flow varies linearly between its bottom and (zero) surface value, such that the horizontal mass flux is divergenceless. This enables us to evaluate the vertically uniform flow in response to an impulsively rotating tank in terms of the mass transport stream function. In the case that the tank width, L, approaches its depth H_0, the topographically induced flow becomes more complicated and this case is discussed in §4.3 for slender tanks ($\delta \gg 1$). Finally, there is one class of geometries in which the cross-slope lengthscale B equals the change in depth, ΔH (such that $\alpha = 1$ and $\gamma = \delta$), which can be solved for arbitrary alongslope lengthscale L. This will be discussed in §4.4.

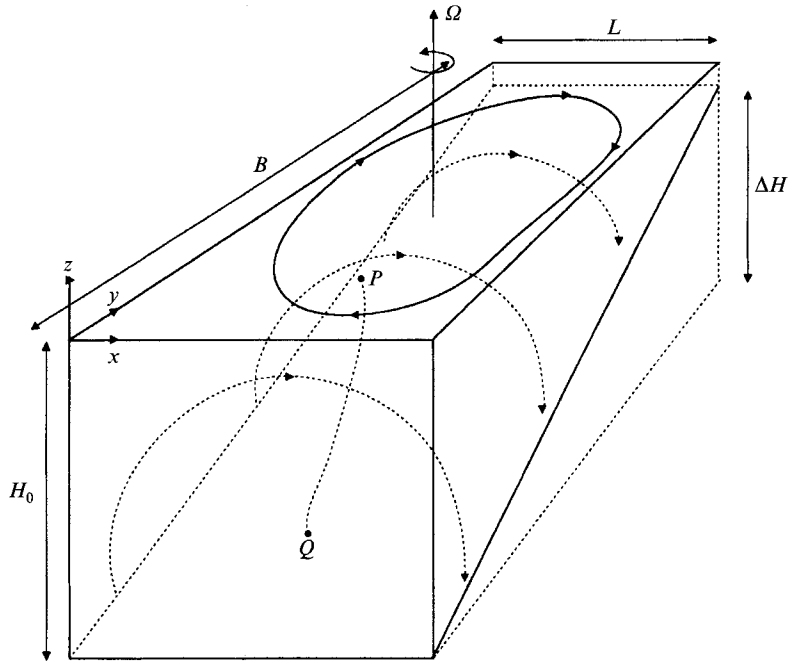

FIGURE 8. Schematic picture of the inviscid response in a rotating tank (angular velocity Ω) with sloping bottom (depth difference ΔH). The non-axisymmetric tank configuration produces, by conservation of vorticity, the depth-independent anticyclonic stream-function flow (denoted by a solid line at the surface), symmetric with respect to the tank axes. The cross-slope flow in turn drives a potential flow (dotted lines) which contributes a near-surface flow in the positive x-direction. Depending on the degree of bottom trapping (which is determined by the vertical aspect ratio γ) this moves the surface position of the cell centre (position P) to the deeper region. As the return flow is stronger near the bottom this stagnation point (Q) has been displaced even further. The complete stagnation line has been depicted schematically by the dotted curve PQ.

4.1. *Equations governing the inviscid spin-up*

The steady Euler equations in a frame of reference rotating anticlockwise with angular velocity Ω about the z-direction (unit vector $\hat{\boldsymbol{k}}$) are given by

$$(\boldsymbol{\omega}+2\Omega\hat{\boldsymbol{k}})\times\boldsymbol{u} = -\boldsymbol{\nabla}(p/\rho+\tfrac{1}{2}\boldsymbol{u}\cdot\boldsymbol{u}+gz), \tag{3}$$

$$\boldsymbol{\nabla}\cdot\boldsymbol{u} = 0, \tag{4}$$

where $\boldsymbol{u} = (u, v, w)$ denotes the velocity components in the x-, y- and z-directions of a Cartesian frame, respectively. Here p is the pressure, ρ the uniform density and g the acceleration due to gravity, directed downwards along the z-axis.

At solid boundaries the normal velocity vanishes:

$$\boldsymbol{u}\cdot\boldsymbol{n} = 0, \tag{5}$$

where $\boldsymbol{n}$ denotes the unit normal vector at the boundary. In the present experiments the upper surface is free. The variations in the free surface, however, are small when the Froude number, defined in (1*e*), is small and (5) can be applied at $z = 0$ as well.

Since there is no production of vorticity in the inviscid starting phase, the absolute vorticity is conserved, i.e. equal to its (zero) value prior to the spin-up:

$$\boldsymbol{\omega}+2\Omega\hat{\boldsymbol{k}} = 0. \tag{6}$$

From (3) one derives the Bernoulli integral

$$p/\rho+\tfrac{1}{2}\boldsymbol{u}\cdot\boldsymbol{u}+gz = \text{constant},$$

which determines the pressure at each position in the fluid.

The starting flow is thus governed by (4) and (6) subject to the constraint (5). The general solution is determined by a combined three-dimensional potential, ϕ, and a two-dimensional stream function, ψ:

$$u = \phi_x - \psi_y, \quad v = \phi_y + \psi_x, \quad w = \phi_z, \tag{7}$$

where the subscript-derivative convention is used.

From (4) and (6), ψ and ϕ have to obey

$$\Delta_2 \psi = -2\Omega, \quad \Delta_3 \phi = 0, \tag{8a, b}$$

with Δ_2 and Δ_3 denoting the (horizontal) two- and three-dimensional Laplacian operators, respectively. The boundary conditions at horizontal and vertical boundaries are

$$\psi = \phi_n = 0, \tag{9a}$$

where ϕ_n denotes the derivative of ϕ normal to the boundary and, at sloping boundaries,

$$(\nabla\phi + \hat{\boldsymbol{k}} \times \nabla\psi) \cdot \boldsymbol{n} = 0. \tag{9b}$$

The 'forcing', at the right-hand side of (8*a*), is thus via the stream-function field, resulting in motions in the plane normal to the rotation axis. The potential flow is entirely due to cross-slope motion at sloping boundaries, see (9*b*).

In the experiments considered in the present paper the tank has a rectangular shape. Its boundaries are given by $x = 0, L$ and $y = 0, B$. The surface, at $z = 0$, is now assumed to be flat (rigid), while the bottom, at $z = -H(y)$, is linearly sloping and given by

$$H(y) = H_0(1 - \alpha y/B). \tag{10}$$

For this particular problem the boundary conditions read

$$\psi = 0 \quad \text{at} \quad x = 0, L \quad \text{and} \quad y = 0, B; \tag{11a}$$

$$\phi_x = 0 \quad \text{at} \quad x = 0, L; \tag{11b}$$

$$\phi_y = 0 \quad \text{at} \quad y = 0, B; \tag{11c}$$

$$\phi_z = 0 \quad \text{at} \quad z = 0; \tag{11d}$$

$$\phi_z = -(\phi_y + \psi_x) H_y \quad \text{at} \quad z = -H(y). \tag{11e}$$

The explicit analytic solution of the three-dimensional potential field is usually limited by the (non-) existence of the Green's function for a particular geometry. Indeed, even for the simple linearly sloping boundary, treated presently, such an explicit solution exists only for the specific case that the bottom slopes right up to the surface ($\alpha = 1$) and has a slope $\varphi = 45°$ (such that $B = \Delta H$). This case is discussed in §4.4. In the next two sections two idealizations will be made that allow an approximate determination of the flow field.

4.2. *The starting flow in a shallow tank: $\gamma^2 \ll 1, \delta = O(1)$*

After proper scaling and expansion of the velocity field in the small vertical aspect ratio (squared), (4) and (6) yield the classical shallow-water result that the horizontal flow is vertically uniform. The horizontal transport, to lowest order, is consequently non-divergent:

$$\frac{\partial}{\partial x}(uH) + \frac{\partial}{\partial y}(vH) = 0 \tag{12}$$

and allows the introduction of a transport stream function Ψ according to

$$Hu = -\frac{\partial \Psi}{\partial y}, \quad Hv = \frac{\partial \Psi}{\partial x}. \tag{13}$$

Inserting this in the equation expressing the conservation of vertical vorticity

$$\frac{\partial v}{\partial x}-\frac{\partial u}{\partial y}=-2\Omega \tag{14}$$

yields

$$\nabla^2\Psi-\frac{1}{H}(\nabla H\cdot\nabla\Psi)=-2\Omega H, \tag{15}$$

with ∇ now denoting the horizontal two-dimensional gradient. This equation is solved subject to the requirement that

$$\Psi=0 \quad \text{at} \quad x=0,L \quad \text{and} \quad y=0,B. \tag{16}$$

Inserting the specific linearly sloping bottom profile (10), the equation describing the shape of the transport stream function associated with the starting flow in a shallow tank is given by

$$\nabla^2\Psi+\frac{\alpha}{1-\alpha y/B}\frac{\partial\Psi}{\partial y}=2\Omega\left(\frac{\alpha y}{B}-1\right)H_0. \tag{17}$$

Approximate solution for small bottom slopes ($\alpha \ll 1$)

Before turning to an exact solution of (17) it is useful to consider the approximation of a nearly flat bottom: $\alpha=\Delta H/H_0\to 0$, for which (17) takes a relatively simple form:

$$\nabla^2\Psi+\alpha\Psi_y=-2\Omega H_0 \quad (\alpha\ll 1). \tag{18}$$

This is particularly relevant as the limit $\alpha\to 0$ is hard to assess in the subsequent solution for arbitrary values of α.

After finding a particular solution of (18), the method of separation of variables can be applied to solve the homogeneous equation (subject to inhomogeneous boundary conditions). This solution procedure is straightforward, and yields

$$\Psi(x,y)=-\tfrac{1}{2}\Omega(x^2-xL)-\frac{4\Omega L^2}{\pi^3}\sum_{n=0}^{\infty}\left\{\frac{\sin(2n+1)\pi x/L}{(2n+1)^3}\right.$$
$$\left.\times\left[e^{-\frac{1}{2}\alpha(y/B-1)}\sinh d_n\, y/B+e^{-\frac{1}{2}\alpha y/B}\sinh d_n(1-y/B)\right]/\sinh d_n\right\}, \tag{19a}$$

with

$$d_n=(\tfrac{1}{4}\alpha^2+(2n+1)^2\pi^2\delta^2)^{\frac{1}{2}}. \tag{19b}$$

Note that in the limit $\alpha\to 0$ this solution correctly approaches that for the flat-bottom case presented by vHDD.

The streamline pattern according to this solution shows a large cell that fills the domain completely. This cell is symmetric about the line $x=\frac{1}{2}L$, and shows a weak asymmetry about the line $y=\frac{1}{2}B$. The weakness of this asymmetry is due to the small value of α, to which (22) is restricted. For values $\alpha=O(1)$, the solution (19) shows a pattern that resembles the observed starting flow (see figure 3) to a remarkable degree, but such a comparison lacks a physical basis. Instead, we return to the original equation (17) in order to derive an exact analytical solution.

Exact solution

The general solution of (17) for the linearly sloping topography (10) is, for arbitrary values of α, given by (see Appendix A)

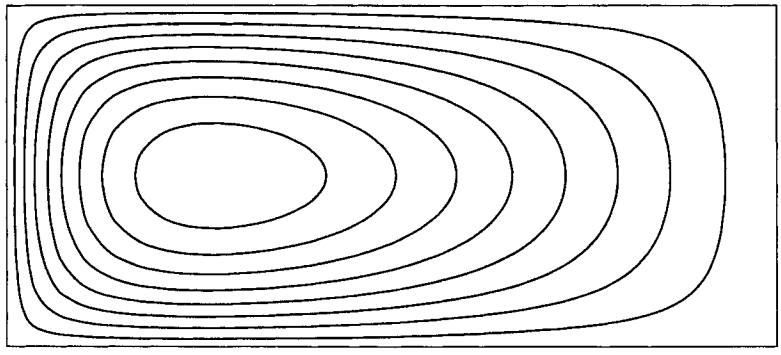

FIGURE 9. Streamline pattern according to (20*a*) for the case $\delta = 2.28$, $\alpha = 0.92$, $\gamma^2 \to 0$.

$$\Psi = \Omega B^2 y\left[\frac{1-y/B}{\alpha-2}+\frac{\alpha}{3}\left(\frac{y}{B}-\frac{y^2}{B^2}\right)\right]$$
$$+\frac{\pi^2}{2}\Omega B^3\sum_{n=0}^{\infty}\frac{\cosh(\lambda_n\alpha/B)(x-\frac{1}{2}L)}{\cosh(\frac{1}{2}\lambda_n\alpha L/B)}\left(1-\frac{\alpha y}{B}\right)\left\{Y_1(\lambda_n)J_1\left(\lambda_n\left(1-\frac{\alpha y}{B}\right)\right)\right.$$
$$\left.-Y_1\left(\lambda_n\left(1-\frac{\alpha y}{B}\right)\right)J_1(\lambda_n)\right\}\frac{1}{\lambda_n^2}$$
$$\times\left[\frac{J_1(\lambda_n)}{J_1(\lambda_n(1-\alpha))}H_1(\lambda_n(1-\alpha))-H_1(\lambda_n)\right]\Big/\left[\frac{J_1^2(\lambda_n)}{J_1^2(\lambda_n(1-\alpha))}-1\right], \tag{20a}$$

with λ_n determined by

$$J_1(\lambda)\,Y_1(\lambda(1-\alpha))-J_1(\lambda(1-\alpha))\,Y_1(\lambda)=0. \tag{20b}$$

Here J_1 and Y_1 are first-order Bessel functions and H_1 is the Struve function.

For the case $\alpha = 1$ and eigenvalues $\lambda_n = \gamma_{1,n}$ (the zeros of the first-order Bessel function of the first kind) the series expression is a regular Fourier–Bessel series, and the solution reads

$$\Psi = -\tfrac{1}{3}\Omega B^2 y\left(1-\frac{y}{B}\right)^2$$
$$+\pi\Omega B^3\sum_{n=0}^{\infty}\frac{\cosh(\lambda_n\alpha/B)(x-\frac{1}{2}L)}{\cosh(\frac{1}{2}\lambda_n\alpha L/B)}\left(1-\frac{y}{B}\right)J_1\left(\lambda_n\left(1-\frac{y}{B}\right)\right)\frac{H_1(\lambda_n)}{\lambda_n^3 J_0(\lambda_n)}. \tag{21}$$

The streamline pattern of the starting flow according to the exact solution (20) is plotted in figure 9 for the particular case $\delta = 2.28$, $\alpha = 0.92$, which corresponds to the experiment shown in figure 2. In agreement with the experimental observations, the theoretical flow pattern shows a marked asymmetry, with the highest streamline density in the deeper part of the flow domain. In order to quantify the degree of asymmetry, the scaled position $\hat{y}/B$ of the cell centre has been plotted in figure 10 as a function of the depth ratio $\alpha = \Delta H/H_0$ for the case $\delta = 2.28$. In the extreme case $\alpha = 1$ the position of the cell centre is given by $\hat{y}/B = 0.2599$, whereas for $\alpha = 0$ it lies at $\hat{y}/B = 0.5$, as was to be expected.

By differentiation of the stream function (20*a*) one derives expressions for the velocity components u, v in the x, y-directions, respectively. The scaled velocity

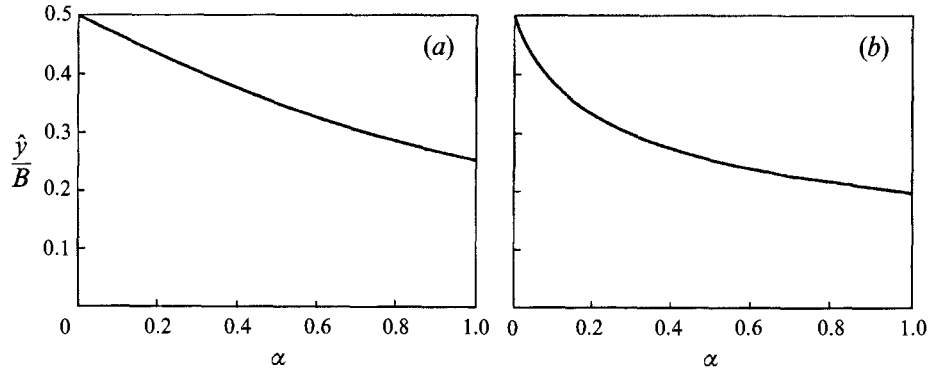

FIGURE 10. Graph showing the scaled position $\hat{y}/B$ of the cell centre as a function of α for the cases $\delta = 2.28$ (a) and $\delta = 4.0$ (b), according to the theoretical solution (20a).

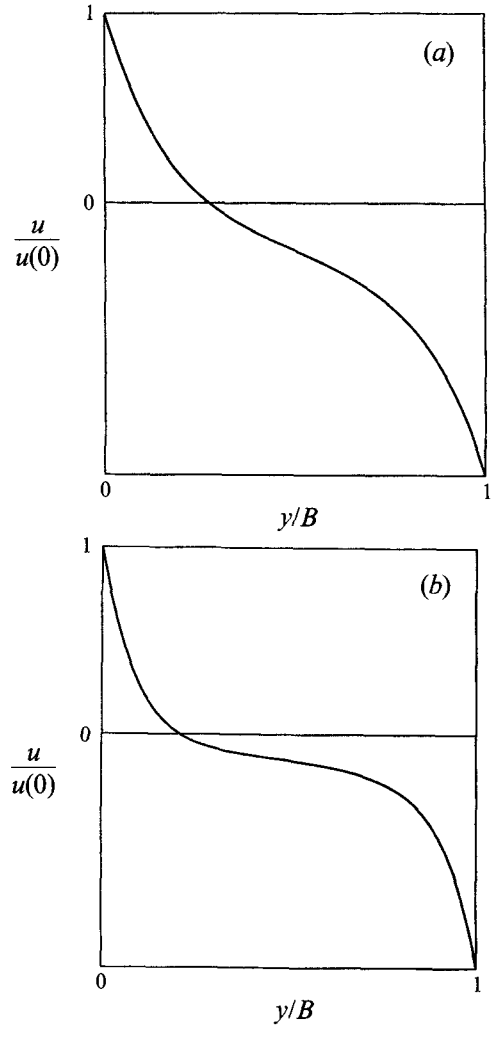

FIGURE 11. Graphs showing the distribution along the axis $x = \frac{1}{2}L$ of the scaled velocity $u/u(0)$ as derived from (20a). Parameter values: (a) $\delta = 2.28$, $\alpha = 0.92$, (b) $\delta = 4.0$, $\alpha = 0.89$.

distribution $u(y/B)/u(0)$ along the symmetry axis $x = \frac{1}{2}L$ is plotted in figure 11 for the cases (*a*) $\delta = 2.28$, $\alpha = 0.92$ and (*b*) $\delta = 4.0$, $\alpha = 0.89$. Obviously, this velocity component has extreme values at the endwalls of the tank, with the largest value (in an absolute sense) occurring in the shallow end; the value 0 corresponds with the centre of the flow cell. It can be seen, in particular from the plot for the larger aspect ratio (figure 11*b*), that the velocity profile is rather flat on the 'shallow side' of the cell centre, while large gradients are present near the endwalls. It should be kept in mind that the solution of the starting flow as discussed in this section allows free slip at the lateral boundaries. In reality, however, thin shear layers will develop at the flow boundaries through which the no-slip condition at the walls is satisfied.

The analysis above, giving the vertically uniform flow, is the zeroth-order term of an infinite sequence of contributions. As such it applies only to very shallow regimes. However, both the parameter values in the experiments (figure 2–7), and the observed variations in positions of the cell centre at the surface (§5) show that a depth-independent theory is not adequate to cover all observed phenomena. Although the next-order (γ^2) depth-dependent velocity components can be calculated in principle it is more fruitful to consider a complementary class of problems in which the vertical aspect ratio, γ, is now assumed to be $O(1)$, but for which the horizontal aspect ratio is large, i.e. $\delta \gg 1$.

4.3. *The starting flow in a slender tank: $\delta \gg 1$, $\gamma = O(1)$*

The solution of the Poisson equation (8*a*), subject to the boundary condition (11*a*), is (for arbitrary horizontal aspect ratio) given by vHDD and (19) with $\alpha = 0$; here it is expressed in the slightly different form

$$\psi = \Omega x(L-x) - \frac{8\Omega}{L}\sum_{i=0}^{\infty}\frac{\cosh\mu_i(y-\frac{1}{2}B)}{\cosh\mu_i\frac{1}{2}B}\frac{\sin\mu_i x}{\mu_i^3}, \tag{22}$$

with

$$\mu_i = (2i+1)\pi/L. \tag{23}$$

From this the cross-slope flow v_s is obtained as

$$v_s \equiv \psi_x = (L-2x)\Omega - \frac{8\Omega}{L}\sum_{i=0}^{\infty}\frac{\cosh\mu_i(y-\frac{1}{2}B)}{\cosh\mu_i\frac{1}{2}B}\frac{\cos\mu_i x}{\mu_i^2}, \tag{24}$$

which is antisymmetric with respect to $x = \frac{1}{2}L$. Expressing the linearly varying part in v_s in a similar infinite series (Oberhettinger 1973) the cross-slope velocity can also be expressed as a single infinite cosine series, facilitating the subsequent analysis for the potential:

$$v_s = \sum_{i=0}^{\infty} v_s^{(i)}\cos\mu_i x, \tag{25}$$

where

$$v_s^{(i)} \equiv \frac{8\Omega}{L\mu_i^2}\left(1 - \frac{\cosh\mu_i(y-\frac{1}{2}B)}{\cosh\mu_i\frac{1}{2}B}\right). \tag{26}$$

It is this cross-slope flow that is driving the potential flow (boundary condition (11*e*)). Lacking a general expression for the Green's function of the potential problem (8*b*) with boundary conditions (11*b–e*) it is at this point that some additional assumption has to be made. In this section it is assumed that $H, L \ll B$ ($\delta \gg 1$). Equations (8*b*) and (11*b–e*) then simplify to a Neumann problem (in which the flux, $\nabla\phi$, is specified at the

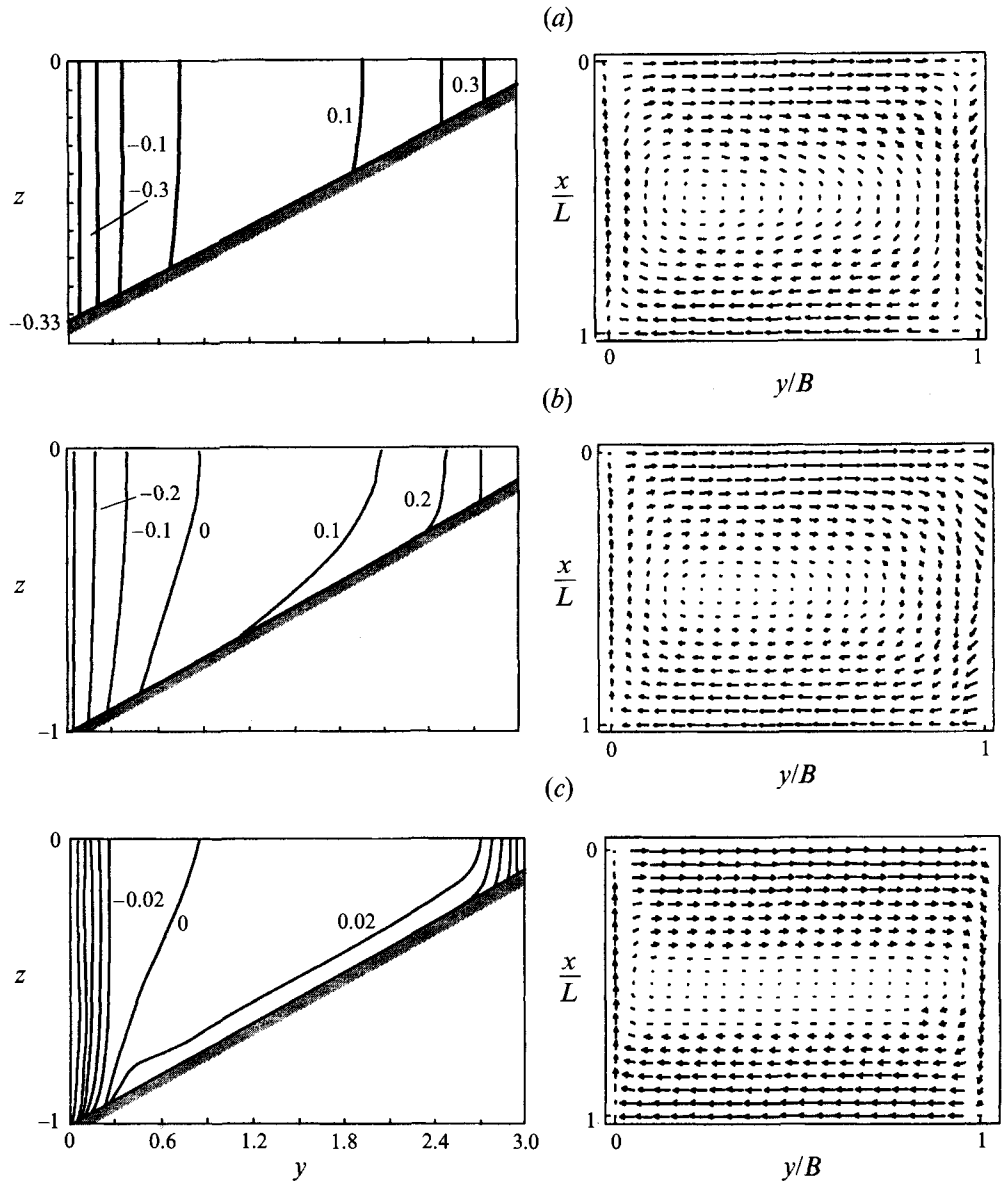

FIGURE 12. Left: cross-sectional view of the normal velocity u, positive, i.e. out of the paper in the x-direction, at $x = \frac{1}{2}L$, the plane of symmetry. Right: top view of the surface circulation in a slender tank ($B = 3$, $\alpha = 0.9$) for (*a*) $\gamma = \frac{1}{3}$ ($H_0 = \frac{1}{3}, L = 1$), (*b*) $\gamma = 1$ ($H_0 = 1, L = 1$) and (*c*) $\gamma = 3$ ($H_0 = 1$, $L = \frac{1}{3}$). Note that the aspect ratios of the figures are not on scale.

boundary) in a rectangle (whose 'depth' decreases parametrically with increasing y-position):

$$\left(\frac{\partial^2}{\partial x^2}+\frac{\partial^2}{\partial z^2}\right)\phi = 0; \tag{27a}$$

$$\phi_x = 0 \quad \text{at} \quad x = 0, L; \tag{27b}$$

$$\phi_z = 0 \quad \text{at} \quad z = 0; \tag{27c}$$

$$\phi_z = -\psi_x H_y \quad \text{at} \quad z = -H(y). \tag{27d}$$

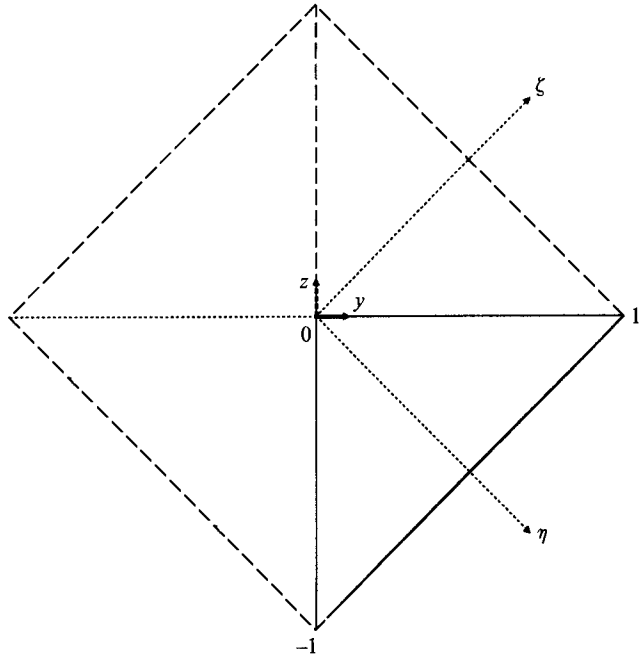

FIGURE 13. Wedge-shaped region (solid lines) and virtual, triangular regions (dashed lines) in the (y, z)-plane. Original (y, z) and rotated (η, ζ) coordinate systems.

Owing to the antisymmetry with respect to the $x = \frac{1}{2}L$ plane the boundary-forcing term in (27*d*) satisfies Neumann's compatibility condition (Zauderer 1989, p. 459), which requires that the line integral of the boundary forcing should vanish. Physically this is merely a condition that total mass is to be conserved, which is obviously satisfied.

The solution of (27) can be obtained by employing the modified Green's function for a rectangle (Zauderer 1989, p. 463). Convolution with the forcing term yields

$$\phi = 8\alpha \frac{H_0 \Omega}{LB} \sum_{i=0}^{\infty} \frac{\cosh \mu_i z}{\sinh \mu_i H} \frac{\cos \mu_i x}{\mu_i^3} \left(\frac{\cosh \mu_i (y - \frac{1}{2}B)}{\cosh \mu_i \frac{1}{2}B} - 1 \right), \tag{28}$$

with $H(y)$ given by (10). From (7), (22) and (28) the approximate three-dimensional velocity structure is obtained. In figure 12 contours of the u-velocity in the plane of symmetry $x = \frac{1}{2}L$ (where both other velocity components vanish), and a top view of the surface circulation are given. As is clear from this figure the solution is close to vertically uniform in the case $\gamma = \frac{1}{3}$, $\delta = 3$, see figure 12(*a*). Numerical evaluation of the series expressions in the velocity field for these parameter values shows that the velocity field approaches the two-dimensional velocity field of §4.2 (in the limit $\gamma^2 \to 0$). For large values of γ^2 ($\gamma = 3$, $\delta = 9$, see figure 12*c*) the velocity field is bottom-intensified. The corresponding surface circulation changes from asymmetric, with the cell centre shifted towards the deeper side of the basin, to symmetric. Notice that this zeroth-order velocity field fails to represent the velocity structure correctly at the shallow side of the basin ($y \to B$). The location of the stagnation line ($u = 0$) also creates the wrong impression that the location of the cell centre and hence the asymmetry increases with decreasing lengthscale L. As the surface velocity field in figure 12(*c*) shows, the flow is

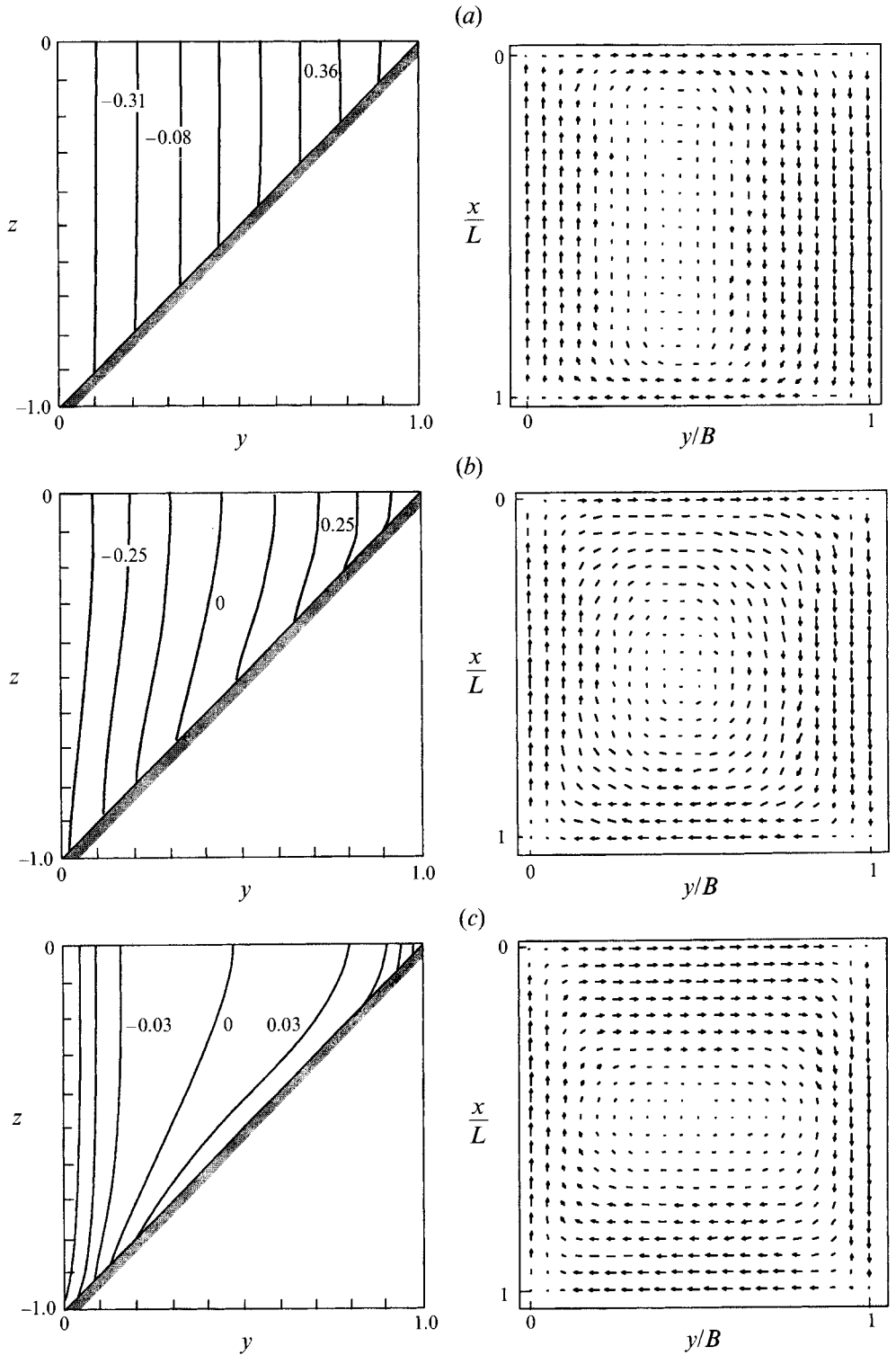

FIGURE 14. As figure 12 but with $\Delta H = H_0 = B = 1$ for (*a*) $\gamma = \frac{1}{3}$ ($L = 3$), (*b*) $\gamma = 1$ ($L = 1$) and (*c*) $\gamma = 3$ ($L = \frac{1}{3}$).

basically symmetric at $L = \frac{1}{3}$, the artificial small value of the location of the cell centre being corrected for by the higher-order solution (figure 15).

Owing to the approximations involved neither the solution in the previous section nor that in the present one is able to simultaneously satisfy both differential equations (8) as well as all of the boundary conditions (11). One single exception, alluded to before, will be considered now.

4.4. *The starting flow in a wedge-shaped container:* $\alpha = 1$, $\gamma = \delta$

When the bottom-slope angle $\varphi = 45°$ the problem to be solved is symmetrical and can be extended by adding virtual triangular regions so as to produce a solid of square cross-section (figure 13). In order to retain the symmetry (and thus be able to guarantee that the no-flux boundary conditions at $y = 0$ and $z = 0$ are satisfied) the normal gradient of ϕ, ϕ_n, at each of the sloping sides of the added triangles is taken to be equal to the boundary forcing in (11*e*), determined by $-\psi_x H_y$. Since $\Delta H = H_0 = B$ this length is taken as the scaling length and the remaining lengthscale L is expressed in terms of it. Also the stream function and potential will be scaled by $2\Omega B^2$.

Prior to solving the Laplace equation for the potential it is convenient to rotate coordinates and introduce (see figure 13):

$$\eta = y - z, \quad \zeta = y + z, \tag{29}$$

where the coordinate η is not to be confused with the free-surface elevation. In view of the simple series form of the forcing (25), (26), a similar series expression is adopted for the potential

$$\phi = \sum_{i=0}^{\infty} \phi^{(i)} \cos \mu_i x. \tag{30}$$

Substituting this into the Laplace equation one has to solve

$$\phi^{(i)}_{\eta\eta} + \phi^{(i)}_{\zeta\zeta} - \mu_i^2 \phi^{(i)} = 0, \tag{31}$$

subject to the boundary conditions

$$\phi^{(i)}_{\eta} = \mp \tfrac{1}{2} v_s^{(i)}(\zeta) \quad \text{at} \quad \eta = \pm 1, \tag{32a}$$

$$\phi^{(i)}_{\zeta} = \mp \tfrac{1}{2} v_s^{(i)}(\eta) \quad \text{at} \quad \zeta = \pm 1. \tag{32b}$$

The solution of this problem is standard and can be obtained from the Green's function in a rectangle (see Appendix B). The potential thus acquires the following expression, symmetric in η and ζ:

$$\phi = \frac{2\Omega}{L} \sum_{i=0}^{\infty} \frac{\cos \mu_i x}{\mu_i} \left\{ \tanh \mu_i / 2 \sum_{n=0}^{\infty} \epsilon_n \right.$$

$$\left. \times \frac{\cos n\pi(\zeta+1) \cosh \nu_{in} \eta + \cos n\pi(\eta+1) \cosh \nu_{in} \zeta}{(n^2\pi^2 + (\mu_i/2)^2) \nu_{in} \sinh \nu_{in}} - \frac{2(\cosh \mu_i \zeta + \cosh \mu_i \eta)}{\mu_i^2 \sinh \mu_i} \right\}, \tag{33a}$$

with μ_i given by (23) and

$$\nu_{in}^2 = n^2\pi^2 + \mu_i^2, \tag{33b}$$

while Neumann's number is denoted as

$$\epsilon_n = \begin{cases} 1, & n = 0 \\ 2, & n = 1, 2, 3, \ldots. \end{cases} \tag{33c}$$

Equations (7), (22), (29) and (33) together determine the complete structure in the wedge-shaped domain. Figure 14 is similar to figure 12 except that the velocity field is

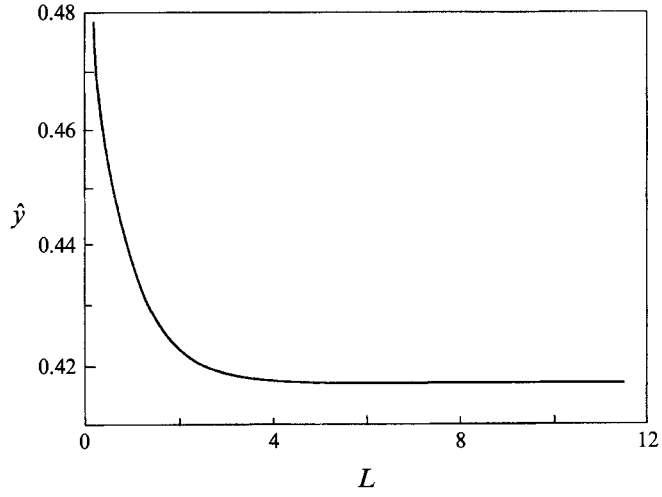

FIGURE 15. The cell-centre position $\hat{y}$ at the surface ($z = 0$) for $\Delta H = H_0 = B = 1$ as a function of dimensionless along-slope lengthscale L.

correctly parallel to the horizontal boundaries everywhere now. As before, the solution varies for decreasing alongslope lengthscale between vertically uniform to bottom-intensified, with an associated surface circulation pattern which varies from asymmetric to symmetric. The decrease of the cell-centre position at the surface with increasing alongslope lengthscale is shown graphically in figure 15.

5. Discussion of observations and comparison with analytical results

5.1. *The starting flow*

The observed starting flow, as visualized in the streak photograph of figure 2, appears to agree very well with the theoretical streamline pattern of the initial flow, see figure 9. A quantitative comparison between theory and experiment is given in figure 16, in which the measured velocity distribution $u(y/B)/u(0)$ along the symmetry axis of the initial flow cell ($x = \frac{1}{2}L$) is plotted together with the theoretical profile, according to (20), for the case $\delta = 2.28$. It is clear that the agreement between the experimental data and the theory is very good, even close to the endwalls of the tank ($y/B = 0$ and 1). Obviously, the various boundary layers at the tank walls are still very thin at this stage, so that the starting flow can indeed be described in the potential-like approach discussed in the beginning of §4.

Another comparison between theory and experiment is given in figure 17, in which the observed positions of the cell centre are plotted as a function of the depth ratio α, together with the theoretical curve, for two sets of experiments, (*a*) $\delta = 2.28$ and (*b*) $\delta = 4.0$. Although the tendency of the experimental data to lie at increasing distance below the line $\hat{y}/B = 0.5$ for larger α-values is observed in both graphs, the numerical values of the data points show a systematic deviation from the theoretical values: all the data points lie above the theoretical curves. The deviation is due to the fact that the theoretical curve, obtained from (20), has been derived for very shallow basins only. A correction for the situation where the transversal lengthscale, L, matches the depth scale H_0, has not been attempted in the present study, but the results of §§4.3 and 4.4 strongly suggest that this theoretical curve gives an upper bound of the cell-centre displacement only. The true displacement, then, will be less and in fact vanishes for increasing vertical aspect ratio γ (see figure 15).

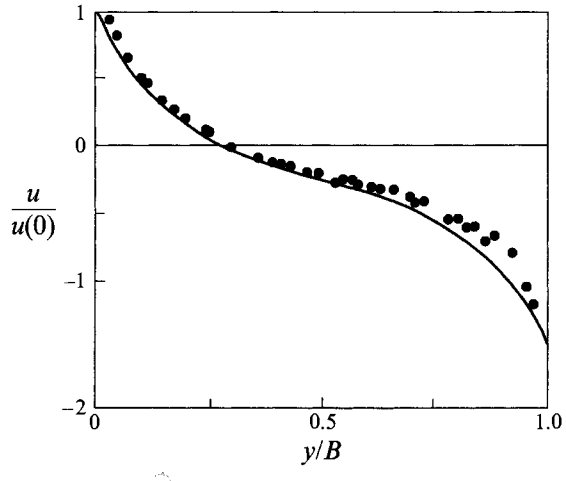

FIGURE 16. As figure 11, with the dots (●) representing measured values. Parameter values: $\delta = 2.28$, $\alpha = 0.92$.

5.2. *Cell formation vs. irregular flow*

As described in §3, the viscous production of vorticity in the lateral boundary layers leads to the creation of cyclonic cells, which quickly distort the initial anticyclonic cell of the starting flow. It was seen that under certain conditions the interaction of the various cells results in a quasi-steady regular array of cells of alternating circulations (see figures 3 and 6), similar to what was observed by vHDD in the case of a tank with a non-sloping bottom. In other cases, however, such an organization into cells is *not* observed (see figures 4, 5 and 7), and the flow remains irregular until eventually all relative motions have decayed due to the spin-up/spin-down mechanism provided by the Ekman layer at the bottom of the container.

In a recent study of barotropic vortices over topography in a rotating tank, Carnevale, Kloosterziel & van Heijst (1991) demonstrated – both experimentally and numerically – that vortices show a substantial drift owing to the topographic forcing. They investigated a variety of bottom topographies and showed that in general cyclonic vortices show a drift in the local 'north-west' direction (north being defined as the direction of maximum upward bottom slope), i.e. they climb the topography under a certain angle. In contrast, anticyclonic vortices show a tendency to translate in the local 'south-west' direction. It is anticipated that this topography effect is also a major factor in the spin-up flows considered in the present paper, in the sense that the different topography-induced drift motions of the cyclonic and anticyclonic cells can destroy a regular cellular array (or prevent its formation), provided that the topography is sufficiently steep. In order to find out if there is some critical topography steepness in the cell formation process, a number of experiments were carried out for different values of the aspect ratio δ and the depth ratio α. The results are presented in figure 18, with the black dots representing experiments in which cell organization was observed, and the open circles representing experiments in which no such organization occurred. For brevity, these cases are also referred to as being 'stable' and 'unstable', respectively. Cases in which this distinction was not clear are indicated by plus signs. It should be noted that the experiment presented in figure 3 ($\delta = 3$, $\alpha = 0.66$), in §3 discussed as an example of a 'stable' case, is marked in figure 18 as an indeterminate case. This experiment is denoted as 'indeterminate' because repeated runs for the same experimental parameter values revealed both organized and non-

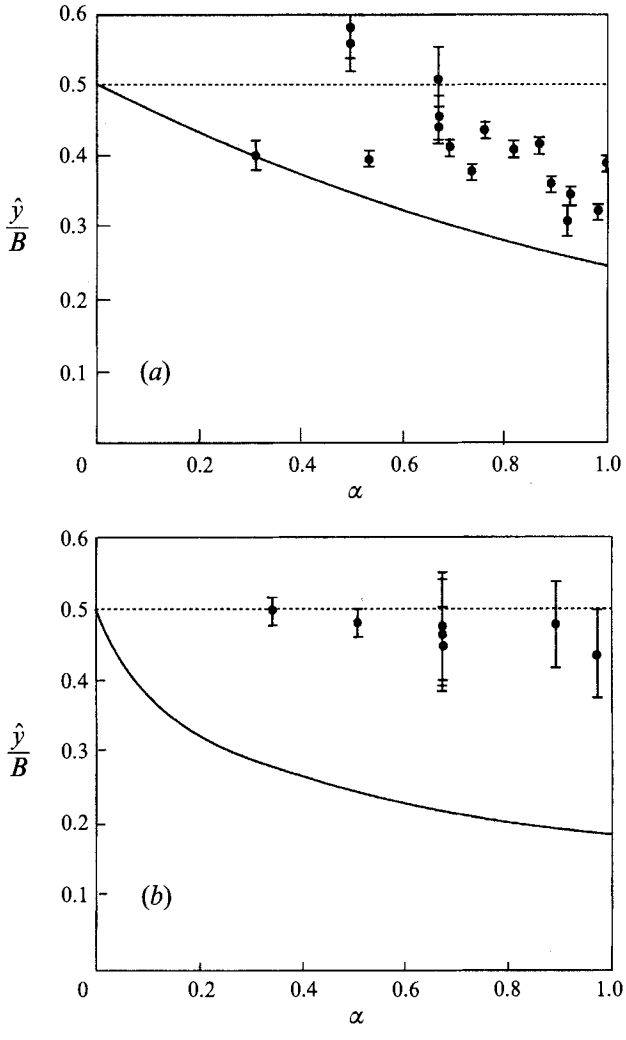

FIGURE 17. As figure 10, with the dots (●) representing experimental data, for (*a*) $\delta = 2.28$ and (*b*) $\delta = 4.0$.

organized final states. The broken line in figure 18 has been drawn by eye, and marks the boundary between the stable and unstable regimes in the (α, δ)-graph. The results clearly show that the flow is unstable (non-organized) for larger α-values and moderate δ-values, whereas pattern formation occurs for larger values of the aspect ratio δ. In fact, the graph suggests that for $\delta > 5$ the flow is stable, i.e. becomes organized, regardless of the value of α. On the other hand, configurations with smaller δ-values seem to yield unstable flow patterns even for very weak topography. The parameter range $0 < \delta < 1$ corresponds with a physically different situation, i.e. with a bottom sloping in the widthwise direction. Experiments carried out for $\delta = 1$ and 0.43 suggest that for this parameter range there exists some critical value $\alpha = \alpha_c$ above which the flow is unstable, irrespective of the δ-value.

The structure of the stability/instability regimes in the upper part ($\delta > 1$) of the (α, δ)-graph can be qualitatively understood by noting that the flow evolution is governed by two competing effects. One of these is the topography-induced drift of vortices (discussed earlier in this section), which tends to destabilize the flow. On the other

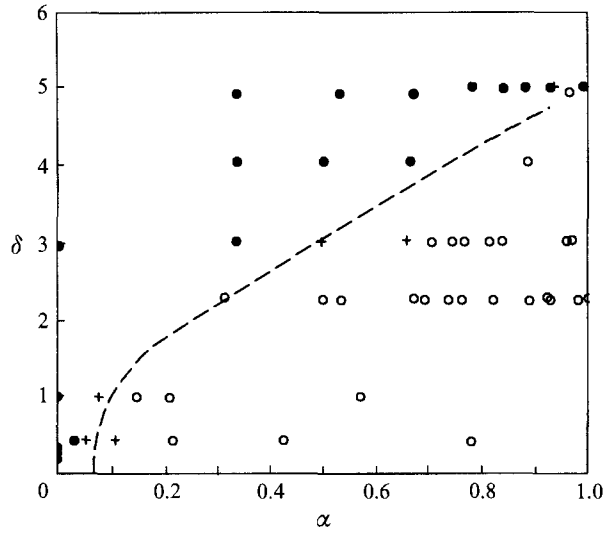

FIGURE 18. Graph showing the type of flow observed in spin-up experiments as a function of the depth ratio α and the aspect ratio δ. The symbol ● refers to experiments in which organization into cells was observed, whereas the symbol ○ refers to experiments in which no cellular pattern was formed. Cases in which the organization was questionable are denoted by the symbol +. The bottom slope $\tan\varphi$ was varied in the range 0.06 to 0.18. The broken line has been drawn by eye.

hand, the (approximately) two-dimensional nature of the flow provides the self-organization mechanism through which the pattern formation occurs. It was found by van Heijst (1989) and by vHDD that the flow cells in the organized state tend to fill the entire domain, and their growth is physically limited by the presence of the lateral boundaries. In the present case, it is the width (L) of the container that provides the upper limit to the cell size. As will be shown later in this section, the cells in the organized state have diameters close to the value of L. Larger values of the aspect ratio δ correspond with a larger number of cells, with diameters that are inversely proportional to δ. Because for a given topography steepness α the smaller cells are likely to be the least affected by the bottom topography, it is then clear that a larger aspect ratio δ stabilizes the flow and thus favours the self-organization into a cellular array. In the spin-up experiments with a flat non-sloping bottom ($\alpha = 0$) as described in vHDD it was found that the number of cells in the organized state is always odd, regardless of the aspect ratio δ of the container. This phenomenon was attributed to the 'topographic' effect of the parabolically shaped upper surface, which causes cyclonic vortices to drift to the centre of the tank. With a cyclonic vortex in the middle, an organized symmetric cell pattern will thus always contain an odd number of cells: for integral odd δ-values, $n = \delta$, whereas for integral even δ-values, n may assume the values $(\delta - 1)$ or $(\delta + 1)$, depending on small perturbations in the initial stages, which affect the subsequent flow evolution towards the cellular array.

In contrast to these observations, the experiments with a sloping-bottom tank in which organization was observed (i.e. with topography steepness α that is sufficiently small to allow organization) revealed that the number of cells is not necessarily odd, and is to a good approximation given by

$$n = \mathrm{env}\,(\delta + 1), \tag{34}$$

provided that $\delta > 1$. Results obtained during 17 experiments with different aspect

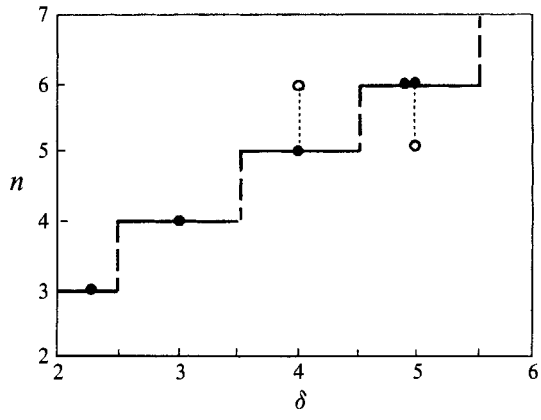

FIGURE 19. Graph showing the observed number of cells (n) as a function of the aspect ratio. The experimental data are denoted by dots (note that the open circles represent single observations, whereas the black dots represent a total of 15 observations), while the solid line designates the relationship $n = \text{env}(\delta+1)$.

ratios ($\delta = 2.28$, 3.0, 4.0, 4.9 and 5.0) are shown graphically in figure 19. It is seen that the number of cells observed for the non-integer δ-values also agree with this step-like function. The open circles each represent a single observation, whereas the black dots represent a total of 15 experiments; for the majority of observations the observed number n thus corresponds with the conjectured relationship very well. Close inspection of the organized flow pattern revealed that a cyclonic cell is not always present in the tank centre, as was the case for $\alpha = 0$. Obviously, the topographic effect imposed by the curved free fluid surface is now overruled by the bottom topography (even for small values of α). Also, it was seen that the largest cells are present in the deeper part of the container (see e.g. figures 3*j* and 6*h*), whereas some smaller cells are crowded together in the shallower part, thus bringing the total number to env $(\delta+1)$.

Once the relationship between the aspect ratio δ and the number of cells is known, it is possible to analyse the stability/instability of the flow as graphically depicted in figure 18. The cases $\delta < 1$ correspond with a sideways sloping bottom, and in the organized flow the cell size D is to a good approximation given by $D \approx B$. Decreasing the δ-value would not affect the organization of the flow; it would only result in a larger number of cells. This implies that in that δ-regime ($\delta < 1$) there exists a critical α-value α_c below which the flow will always become organized, regardless of the δ-value; on the other hand, for $\alpha > \alpha_c$ the flow will remain irregular, without showing any organization. For this reason the line marking the boundary between 'stable' and 'unstable' will be vertical for $\delta \to 0$, and will intersect the α-axis at $\alpha = \alpha_c$.

5.3 *The spin-up timescale*

As was mentioned in §3, in the experiments with steep bottom topography ($\alpha \lesssim 1$) it is observed that the relative flow in the shallow part of the tank shows a rapid decay. This effect can be clearly seen on the subsequent streak photographs of figure 4, 5 and 7. In particular, it can be observed that the region of spun-up fluid steadily increases in time.

A typical timescale for the linear spin-up of a fluid in an axisymmetric container is given by (2). Although this result was derived theoretically for the linear case (see Greenspan & Howard 1963), later studies revealed that this timescale has a wider validity and that it also applies to nonlinear cases, such as spin-up from rest (Weidman

1976*a*, *b*). The Ekman layer in the present geometry has a complicated structure, due both to the sloping bottom and – more seriously – to the highly unsteady, non-axisymmetric flow in the bulk of the fluid domain. For this reason the analysis of the Ekman-layer structure poses a serious problem.

In an attempt to understand the gradual extension of the region of spun-up fluid, it is now assumed that the general spin-up timescale (2) also applies to the present sloping-bottom configuration, with H representing the actual layer depth $H(y) = (1-\alpha y/B)\,H_0$. One thus obtains a spin-up timescale that is essentially dependent on the position y:

$$T_E(y) = (1-\alpha y/B)\,T_E(0), \tag{35}$$

with

$$T_E(0) = 2H_0/(\nu\Omega)^{\frac{1}{2}} \tag{36}$$

the Ekman timescale based on the maximum layer depth H_0.

It is not easy to verify the validity of (35) using the observational results, since the timescale refers to a decay by a factor of e^{-1}, which can only be determined by accurate velocity measurements through the entire flow field; such detailed measurements have not been carried out in the present study. Nevertheless, the y-dependence of the spin-up timescale can be clearly observed from the sequence of streak photographs of the evolving flow field. In particular, (35) predicts the most prominent y-dependence for $\alpha = 1$, which is confirmed by the experiments shown in figures 4, 5 ($\alpha = 0.98$) and 7 ($\alpha = 0.89$). In cases of smaller α-values the y-dependence is much weaker, as can be observed from the photographs shown in figures 3 ($\alpha = 0.66$) and 6 ($\alpha = 0.5$).

In the shallow parts of the tank the spin-up timescale may locally become very small and may thus interfere with the timescale associated with the organization of the flow. Although it is as yet not completely clear how this interference of timescales affects the actual organization process, the observations suggest that the structure of the cells in the organized state (provided the bottom slope is not too steep) is entirely determined by the smallest horizontal lengthscale of the container, i.e. its width. In particular in the slender tank geometries ($\delta > 3$) the relatively rapid spin-up in the shallow part of the container only modifies the cellular pattern locally.

6. Conclusions

Experiments have been carried out in a tank with a linearly sloping bottom which has impulsively been set in rotation. Observations of the (horizontal) surface flow are obtained by means of streak photography by a co-rotating camera. Three principal stages can be discerned in the spin-up process:

(i) inertial, inviscid starting flow consisting of a single gyre which under certain conditions has a displaced cell centre;

(ii) organization of the flow into a number of cells which do or do not, depending on the depth ratio α and the horizontal aspect ratio δ, reach a quasi-steady state;

(iii) subsequent decay of relative motions in cells, or subsequent wandering (and decay) of cells throughout the tank domain (particularly in the deep region).

The inertial flow in the first stage is driven by the conservation of (zero) absolute vorticity in combination with the non-axisymmetric geometry and consists (as in the flat-bottom case) principally of a stream-function flow. This stream-function flow, in turn, drives a potential flow when moving cross-isobath. Vertical penetration of the potential flow is determined by the smallest lengthscale involved. For shallow basins this is the water depth itself and the flow directly contributes to the (observable) surface flow (by displacing the cell centre). Alternatively, for deep basins the potential flow is bottom-trapped and the total flow at the surface is dominated by the symmetric stream-function flow.

The quasi-steady state with multiple cells is, as in the vHDD case, not (yet) physically interpreted, although some information about the stability boundaries in the parameter regime has been determined experimentally.

Appendix A. Solution of equation (17) for arbitrary α

Using

$$x' = x/L - \tfrac{1}{2}, \quad y' = 1 - \alpha y/B, \quad \Psi' = \Omega B^3 \alpha^2 \Psi \tag{A 1}$$

the vorticity equation is, on dropping primes, given by

$$\mu^2 \Psi_{xx} + \Psi_{yy} - (1/y)\, \Psi_y = y, \tag{A 2}$$

with $\mu \equiv \delta/\alpha$, to be solved subject to the condition

$$\Psi = 0 \quad \text{at} \quad x = \pm\tfrac{1}{2}, \quad y = 1, 1-\alpha. \tag{A 3}$$

A particular solution, satisfying the boundary condition at $y = 1, 1-\alpha$ is

$$\psi_p(y) = \tfrac{1}{3}(y-1)\{y-(1-\alpha)\}\{y+(1-\alpha)/(2-\alpha)\}. \tag{A 4}$$

The remaining equation for the homogeneous part, Ψ_h, is solved subject to the condition

$$\Psi_h = 0 \quad \text{at} \quad y = 1, 1-\alpha \tag{A 5}$$

and

$$\Psi_h = -\Psi_p(y) \quad \text{at} \quad x = \pm\tfrac{1}{2}. \tag{A 6}$$

By separation of variables it yields hyperbolic functions in the x-direction and an eigenvalue problem, related to Bessel's equation, in the y-direction. The homogeneous part thus reads

$$\Psi_h = \sum_{n=0}^{\infty} C_n \cosh\left(\frac{\lambda_n x}{\mu}\right) y\, e_n(y), \tag{A 7}$$

where the eigenvalues, λ_n, in this expression are determined by the roots of

$$J_1(\lambda)\, Y_1(\lambda(1-\alpha)) - J_1(\lambda(1-\alpha))\, Y_1(\lambda) = 0. \tag{A 8}$$

The functions $e_n(y)$ in (A 7), given by

$$e_n(y) \equiv Y_1(\lambda_n)\, J_1(\lambda_n y) - J_1(\lambda_n)\, Y_1(\lambda_n y), \tag{A 9}$$

consequently vanish at $y = 1,\ 1-\alpha$ and, moreover, are orthogonal with respect to the weight function y:

$$\int_1^{1-\alpha} y e_n e_m \, \mathrm{d}y = \delta_{nm} \frac{2}{\pi^2 \lambda_n^2} \left\{ \frac{J_1^2(\lambda_n)}{J_1^2(\lambda_n(1-\alpha))} - 1 \right\}, \tag{A 10}$$

with δ_{nm} the Kronecker delta. For $\alpha = 1$ the eigenfunctions reduce to $e_n(y) = J_1(\lambda_n y)$, ensuring regularity at $y = 0$, and the eigenvalues λ_n are the zeros of $J_1(\lambda)$.

The unknown coefficients C_n in the expansion (A 7) of Ψ_h follow by inserting (A 4) and (A 7) in boundary condition (A 6). Subsequently multiplying this by $e_n(y)$ and integrating over the y-domain yields

$$C_n = \frac{1}{\cosh(\lambda_n/2\mu)} \frac{\pi^2}{2\lambda_n^2} \left[\frac{J_1(\lambda_n)}{J_1(\lambda_n(1-\alpha))} H_1(\lambda_n(1-\alpha)) - H_1(\lambda_n) \right] \Big/ \left[\frac{J_1^2(\lambda_n)}{J_1^2(\lambda_n(1-\alpha))} - 1 \right]. \tag{A 11}$$

Here $H_1(z)$ is the Struve function (see Abramowitz & Stegun 1955), p. 495), which vanishes at $z = 0$ and $z \to \infty$ but is positive (though oscillatory) in between.

Appendix B. Solution of Laplace's equation in a wedge-shaped container

The dependency on the index (i) in the eigenvalue μ_i is suppressed by normalizing the potential $\phi^{(i)}$ and the forcing $v_s^{(i)}$ with a constant C, which is obtained from (25), (26) with $B = 1$ by writing the forcing as

$$v_s^{(i)} = C\left(1 - \frac{\cosh \mu_i (y - \tfrac{1}{2})}{\cosh \tfrac{1}{2}\mu_i}\right) \tag{B 1}$$

with

$$C = 8\Omega/(L\mu_i^2).$$

Thus, with

$$\bar{\phi} = \frac{\phi^{(i)}}{C}, \quad \bar{v} = \frac{v_s^{(i)}}{C} \equiv 1 - \frac{\cosh \mu (y - \tfrac{1}{2})}{\cosh \tfrac{1}{2}\mu}, \tag{B 2}$$

one has to solve the following potential problem:

$$\Delta\bar{\phi} - \mu^2\bar{\phi} = 0,$$

$$\bar{\phi}_\eta = \mp\tfrac{1}{2}\bar{v}(\zeta) = \pm\frac{1}{2}\left\{\frac{\cosh \tfrac{1}{2}\mu\zeta}{\cosh \tfrac{1}{2}\mu} - 1\right\} \quad \text{at} \quad \eta = \pm 1,$$

$$\bar{\phi}_\zeta = \mp\tfrac{1}{2}\bar{v}(\eta) = \pm\frac{1}{2}\left\{\frac{\cosh \tfrac{1}{2}\mu\eta}{\cosh \tfrac{1}{2}\mu} - 1\right\} \quad \text{at} \quad \zeta = \pm 1.$$

The modified Green's function of this Neumann's problem for the square is given by

$$K(\eta, \zeta; \eta', \zeta') = \frac{1}{4}\sum_{m,n=0}^{\infty} \epsilon_m \epsilon_n \frac{\cos \lambda_m \tfrac{1}{2}(\eta + 1) \cos \lambda_m \tfrac{1}{2}(\eta' + 1) \cos \tau_n \tfrac{1}{2}(\zeta + 1) \cos \tau_n \tfrac{1}{2}(\zeta' + 1)}{\mu^2 + (\tfrac{1}{2}\lambda_m)^2 + (\tfrac{1}{2}\tau_n)^2},$$

with

$$\lambda_m = m\pi, \quad \tau_n = n\pi$$

and ϵ_n as defined in (33c). The solution is given as a convolution of this Green's function and the boundary forcing (with ds a line-increment of the boundary of the square ∂G):

$$\bar{\phi}(\eta, \zeta) = -\tfrac{1}{2}\int_{\partial G} K(\eta, \zeta; \eta', \zeta')\, \bar{v}(\eta', \zeta')\, \mathrm{d}s$$

$$= -\tfrac{1}{2}\int_{-1}^{1} K(\eta, \zeta; \pm 1, \zeta')\, \bar{v}(\zeta')\, \mathrm{d}\zeta' - \frac{1}{2}\int_{-1}^{1} K(\eta, \zeta; \eta', \pm 1)\, \bar{v}(\eta')\, \mathrm{d}\eta'.$$

Hence one obtains, with (B 2) and (29)

$$\bar{\phi}(\eta, \zeta) = \frac{1}{8}\sum_{m,n=0}^{\infty} \epsilon_m \epsilon_n [\{(-1)^m + 1\} I_n + \{(-1)^n + 1\} I_m] \frac{\cos \lambda_m \tfrac{1}{2}(\eta + 1) \cos \tau_n \tfrac{1}{2}(\zeta + 1)}{\mu^2 + (\tfrac{1}{2}\lambda_m)^2 + (\tfrac{1}{2}\tau_n)^2},$$

where

$$I_n \equiv \int_{-1}^{1} \cos \tau_n \tfrac{1}{2}(\zeta'+1)\left(\frac{\cosh \tfrac{1}{2}\mu\zeta'}{\cosh \tfrac{1}{2}\mu}-1\right)\mathrm{d}\zeta' = \frac{2\mu \tanh \tfrac{1}{2}\mu}{n^2\pi^2+\mu^2}((-1)^n+1)-2\delta_{n0},$$

or, with $n = 2N$,

$$I_N = +\frac{\mu \tanh \tfrac{1}{2}\mu}{N^2\pi^2+(\tfrac{1}{2}\mu)^2}-2\delta_{No}.$$

Hence

$$\bar{\phi}(\eta,\zeta) = \frac{1}{4}\sum_{M,N=0}^{\infty} \epsilon_M \epsilon_N \left(\frac{\mu \tanh \tfrac{1}{2}\mu}{N^2\pi^2+(\mu/2)^2}+\frac{\mu \tanh \tfrac{1}{2}\mu}{M^2\pi^2+(\mu/2)^2}-2\delta_{No}-2\delta_{Mo}\right) \times \frac{\cos M\pi(\eta+1)\cos N\pi(\zeta+1)}{\mu^2+(M^2+N^2)\pi^2}. \quad \text{(B 3)}$$

Evaluating the infinite series expressions with the aid of

$$\sum_{n=0}^{\infty} \frac{\epsilon_n}{b^2+n^2a^2}\cos(n\pi x/L) = \frac{\pi}{ab}\frac{\cosh[(\pi b/aL)(L-x)]}{\sinh(\pi b/a)}, \quad 0 \leqslant x \leqslant 2L$$

(Oberhettinger 1973, equation 1.51) in each of the terms in (B 3), we find

$$\bar{\phi} = \tfrac{1}{4}\mu \tanh \tfrac{1}{2}\mu \left\{ \sum_{M=0}^{\infty} \epsilon_M \frac{\cosh \nu_M \zeta \cos M\pi(\eta+1)}{(M^2\pi^2+(\tfrac{1}{2}\mu)^2)\,\nu_M \sinh \nu_M} + \sum_{N=0}^{\infty} \epsilon_N \frac{\cosh \nu_N \eta \cos N\pi(\zeta+1)}{(N^2\pi^2+(\tfrac{1}{2}\mu)^2)\,\nu_N \sinh \nu_N} \right\} - \frac{(\cosh \mu\zeta+\cosh \mu\eta)}{2\mu \sinh \mu}, \quad \text{(B 4)}$$

where

$$\nu_M^2 = M^2\pi^2+\mu^2.$$

Since N and M are dummies they can be replaced as in (33a) by a single dummy, n, and then the two remaining series can be combined. Reattaching the index (i) to μ, ν and ϕ finally yields expression (33a), when using (B 1), (B 2) and (30).

REFERENCES

Abramowitz, M. & Stegun, I. (Eds.) 1964 *Handbook of Mathematical Functions*. Dover.

Benton, E. R. & Clark, A. 1974 Spin-up. *Ann. Rev. Fluid Mech.* **6**, 257–280.

Carnevale, G. F., Kloosterziel, R. C. & Heijst, G. J. F. van 1991 Propagation of barotropic vortices over topography in a rotating tank. *J. Fluid Mech.* **233**, 119–139.

Greenspan, H. P. & Howard, L. N. 1963 On a time-dependent motion in a rotating fluid. *J. Fluid Mech.* **17**, 385–404.

Heijst, G. J. F. van 1989 Spin-up phenomena in non-axisymmetric containers. *J. Fluid Mech.* **206**, 171–191.

Heijst, G. J. F. van, Davies, P. A. & Davis, R. G. 1990 Spin-up in a rectangular container. *Phys. Fluids* A **2**, 150–159 (referred to herein as vHDD).

Magnus, W., Oberhettinger, F. & Soni, R. P. 1966 *Formulas and Theorems for the Special Functions of Mathematical Physics*, 3rd edn. Springer.

Oberhettinger, F. 1973 *Fourier Expansions*. Academic.

Weidman, P. D. 1976*a* On the spin-up and spin-down of a rotating fluid. Part 1. Extending the Wedemeyer model. *J. Fluid Mech.* **77**, 658–708.

WEIDMAN, P. D. 1976*b* On the spin-up and spin-down of a rotating fluid. Part 2. Measurements and stability. *J. Fluid Mech.* **77**, 709–735.

ZAUDERER, E. 1989 *Partial Differential Equations of Applied Mathematics*. 2nd edn. Wiley Interscience.